

REPORT DOCUMENTATION PAGE

The public reporting burden for this collection of information is estimated to average 1 hour per response, including the time for reviewing the data needed, and completing and reviewing the collection of information. Send comments regarding this burden estimate or any other aspect of this collection of information, including suggestions for reducing the burden, to the Department of Defense, Executive Service Directorate (0704-0188). Respondents should be aware that notwithstanding any other provision of law, no person shall be subject to any penalty for failing to comply with a collection of information if it does not display a currently valid OMB control number.

PLEASE DO NOT RETURN YOUR FORM TO THE ABOVE ORGANIZATION.

1. REPORT DATE (DD-MM-YYYY) 28-09-2009		2. REPORT TYPE Final Performance Report		3. DATES COVERED (From - To) 1 June 2008 - 30 June 2009	
4. TITLE AND SUBTITLE High Frequency Excitation for Cavity Flow Control: Combined Experiments and Linear Stability Analysis				5a. CONTRACT NUMBER FA9550-08-1-0279	
				5b. GRANT NUMBER	
				5c. PROGRAM ELEMENT NUMBER	
6. AUTHOR(S) Raman, Ganesh, G. (Principal Investigator) Sarpotdar, Shekhar, M. Panickar, Praveen				5d. PROJECT NUMBER	
				5e. TASK NUMBER	
				5f. WORK UNIT NUMBER	
7. PERFORMING ORGANIZATION NAME(S) AND ADDRESS(ES) Illinois Institute of Technology Sponsored Research and Programs 3300 South Federal Street, Room 201 Chicago, IL 60616-3792				8. PERFORMING ORGANIZATION REPORT NUMBER OSRP No. 5922	
9. SPONSORING/MONITORING AGENCY NAME(S) AND ADDRESS(ES) USAF, AFRL DUNS 143574726 Air Force Office of Scientific Research 875 North Randolph Street Suite 325, Room 3112 Arlington, VA 22203				10. SPONSOR/MONITOR'S ACRONYM(S) AFOSR/PKR2	
				11. SPONSOR/MONITOR'S REPORT NUMBER(S)	
12. DISTRIBUTION/AVAILABILITY STATEMENT Approved for public release					
<div style="display: flex; justify-content: space-between;"> <div>13. SUPPLEMENTARY NOTES</div> <div style="font-size: 48pt; font-weight: bold;">20100616371</div> </div>					
14. ABSTRACT A rod in cross flow is a technique known for its simple and effective means of suppressing cavity tones. Although several hypotheses have been put forward regarding its working principle, no validated explanation exists. In the present study we investigate whether the cylinder, through its wake, changes the stability characteristics of the shear layer that develops over the cavity. The present study pertains to a shallow cavity of length to depth ratio $L/D = 2$, for subsonic Mach numbers ranging from 0.5 to 0.8. The upstream boundary layer was found to be turbulent for all cases considered. We use linear stability theory in the spatial, compressible and inviscid formulation for our study. We construct artificial velocity profiles that are prototypical of the experimentally measured velocity profiles, to investigate how the wake of the cylinder influences the stability of the shear layer. Comparison of these integrated growth rates with the acoustic suppression data showed that the link between the two is weak. Thus the ability of the rod to suppress cavity resonance is not directly explained by linear stability analysis of the modified shear layer, for the configurations considered.					
15. SUBJECT TERMS Cavity flow control, noise suppression, aircraft bays.					
16. SECURITY CLASSIFICATION OF:			17. LIMITATION OF ABSTRACT	18. NUMBER OF PAGES	19a. NAME OF RESPONSIBLE PERSON
a. REPORT	b. ABSTRACT	c. THIS PAGE			Dr. Ganesh G. Raman
U	U	U	UU	59	19b. TELEPHONE NUMBER (Include area code) (312) 567-3035

Final Performance Report
Contract/Grant No.: FA9550-08-1-0279
Reporting Period: 1 June 2008 to 30 June 2009

High Frequency Excitation for Cavity Flow Control: Combined Experiments and Linear Stability Analysis

Ganesh Raman (Principal Investigator), Shekhar Sarpotdar, and Praveen Panickar
Fluid Dynamics Research Center, Illinois Institute of Technology, Chicago, IL 60616, USA

Abstract

A rod in cross flow is a technique known for its simple and effective means of suppressing cavity tones. Although several hypotheses have been put forward regarding its working principle, no validated explanation exists. In the present study we investigate whether the cylinder, through its wake, changes the stability characteristics of the shear layer that develops over the cavity. The present study pertains to a shallow cavity of length to depth ratio of 2, for subsonic Mach numbers ranging from 0.5 to 0.8. The upstream boundary layer was found to be turbulent for all cases considered. We use linear stability theory in the spatial, compressible and inviscid formulation for our study. We construct artificial velocity profiles that are prototypical of the experimentally measured velocity profiles, to investigate how the wake of the cylinder influences the stability of the shear layer. Comparison of these integrated growth rates with the acoustic suppression data showed that the link between the two is weak. Thus the ability of the rod to suppress cavity resonance is not directly explained by linear stability analysis of the modified shear layer, for the configurations considered.

I. INTRODUCTION

Flows over cavities have been the subject of active research for several decades for the richness of the physics involved and their occurrence in many practical situations. Under certain conditions these flows produce intense acoustic tones, also known as cavity tones, at discrete frequencies. The significance of cavity flows is not just limited to the acoustic fields they produce. The distinctive pressure and velocity fields produced by this phenomenon are of equal importance.

There are a number of practical situations where flows over cavities are a concern. The flow over the wheel-well of an aircraft during take-off or landing is one of the most common examples of such a situation. The study by Heller and Dobrzynski¹ suggested that the wheel-well was an important source of noise during landing approach. As mentioned earlier, it is not just the large acoustic amplitudes, but also the altered flow field that could interfere with the performance of systems placed in the vicinity of the cavity. Under certain conditions, the presence of cavity is found to increase drag (McGregor and White²) and change the aerodynamic as well as stability characteristics of projectiles (Sahoo, Annaswamy and Alvi³). Steep density gradients and vortex-like structures associated with the intense acoustic waves emanating from the cavity are found to interfere with airborne optical systems mounted on aircraft. In ramjet combustors, the coupling between the cavity tones and the combustion dynamics is a serious concern since it may limit the performance of the engine (King, Creel and Bushnell⁴, Najm and Ghoniem⁵). In the case of gas transportation through conduits attached with closed side branches, the cavity instability phenomenon may be manifested in the form of unsteady gas flow (Kriesels *et al.*⁶) and structural vibrations (Martin, Naudascher and Padmanabhan⁷).

II. BACKGROUND AND MOTIVATION

Historical perspectives on the physics of cavity flows can be obtained from the papers of Rockwell and Naudascher⁸ and Chokani⁹; these papers provide a comprehensive review encompassing a range of topics such as classification of the cavity flows, parameters that influence the cavity oscillations, theoretical models and suppression strategies. More recently, the reviews by Cattafesta *et al.*¹⁰ and Rowley and Williams¹¹ have focussed on the

classification and methodology of cavity resonance control techniques.

A. Physical Mechanism

Cavity tones are an example of a self sustained acoustic oscillation phenomenon that relies on the feedback loop comprising of interaction of the unstable shear layer with the aft wall and upstream propagation of acoustic waves towards the leading edge of the cavity. Figure 1 shows the schematic of this acoustic feedback loop. As shown in this figure, when the unsteady shear layer impinges on the downstream edge of the cavity, it gives rise to pressure disturbances. When these pressure disturbances, i.e., acoustic waves, reach the upstream edge of the cavity, they strengthen the nascent shear layer instabilities. Thus, the feedback loop between downstream-traveling hydrodynamic disturbances in the shear layer and the upstream-traveling acoustic disturbances is closed. This feedback loop gives rise to intense acoustic tones of discrete frequency, known as cavity tones. Jet impingement tones (Tam and Ahuja¹²), screech tones (Raman¹³), edge tones (Crighton¹⁴), and ring tones (Howe¹⁵) are some of the other self sustained acoustic oscillations which share the same physical mechanism as the cavity tones.

Some of the earliest predictions of the cavity tone frequency were based on the normal modes of cavity resonance (East¹⁶). However, these predictions were restricted to deep cavities at very low Mach numbers. At higher Mach numbers the cavity tone spectrum showed the presence of multiple tones. These tones were not harmonics of each other, hence could not be explained using normal acoustic modes of the cavity. Powell¹⁷ explained the mechanism of self sustained acoustic resonance within the framework of the acoustic feedback loop. Using the edge tone phenomenon, he argued that the time taken by the large scale structures to reach the edge and time taken by the acoustic waves to propagate back to the nozzle lip should be an integral multiple of the resonant time scale. Any mismatch in time could be reconciled by incorporating a term that accounts for the phase shift between the hydrodynamic and acoustic waves. Rossiter¹⁸ was the first to apply this model to cavity tones. In its mathematical form, the cavity tone resonance frequency is predicted using the following equation:

$$St_L = \frac{fL}{U_+} = \frac{m - \nu}{\frac{1}{\kappa} + M_+ \frac{a_+}{a_-}}. \quad (1)$$

Here, the subscript ‘+’ denotes freestream properties, whereas the subscript ‘-’ denotes properties within the cavity. The coefficient ‘ κ ’ is the ratio of the velocity of the convective disturbance (U_c) and the freestream velocity (U_∞), and ‘ ν ’ is the phase ambiguity between the hydrodynamic and acoustic waves. The model was intended to be semi-empirical in nature, in the sense that the coefficient (κ) was found using experimental measurements, and the constant (ν) was chosen arbitrarily to be a value that best fit experimental data. However, in the absence of experimental measurements to determine the convective velocity, the value of ‘ κ ’ can also be arbitrarily chosen such that the theoretical frequency calculated using equation (1) matches experimental data. Bilanin and Covert¹⁹ made an attempt to calculate the value of κ and ν through a theoretical analysis for Mach numbers ranging between 0.8 and 3. According to them, the presence of two or more non-harmonic frequencies in the cavity tone spectrum can be attributed to the participation of corresponding vortex-sheet displacement modes. Despite the fact that this model was free from any empirical constants, it had some shortcomings. It did not take into account the effect of cavity depth or shear layer thickness. Later, Tam and Block²⁰ extended this model to include the effect of momentum thickness, θ , and aspect ratio, L/D , by taking the reflection of acoustic waves from the floor of the cavity into account.

B. Cavity Resonance Suppression Efforts

There have been numerous documented attempts to suppress resonant cavity tones using various flow control techniques, both passive as well as active²¹ in nature. One of the simplest methods to suppress high amplitude cavity oscillations is to put a spoiler of appropriate height at the leading edge of the cavity. It has been shown that spoilers having saw-toothed shaped upper surfaces which span the entire width of the cavity, physically loft the shear layer, thereby reducing the interaction between the shear layer and cavity downstream edge, thus providing resonance suppression. Early efforts on exploring the efficacy of the cylinder in crossflow as a device to suppress the cavity tones were undertaken by McGrath and Shaw²². Ukeiley *et al.*²³ compared the performance of a simple fence-type spoiler with that of the cylinder in crossflow and found that despite the prominent shear layer lift-off effect produced by the spoiler, the cylinder in crossflow proved to be more efficient in suppressing the cavity tones.

Stanek *et al.*²⁴⁻²⁶ did extensive work on cavity tone suppression using a cylinder in cross-flow. They were able to demonstrate the effectiveness of the cylinder in crossflow as an actuator for wide range of Mach numbers and cavity dimensions. By securing correctly designed end plates, they were able to extend the suppression performance of cylinder beyond the subsonic range of freestream Mach numbers. They also attempted to understand the governing physical mechanism leading to cavity resonance suppression using the cylinder in crossflow. They hypothesized that the resonance suppression resulting from the use of the cylinder in crossflow was due to either (i). Lifting-off of the shear layer, (ii). High frequency forcing of the shear layer, or (iii). Altered stability characteristics of the shear layer. The conjecture of shear layer lift-off was explored by Arunajatesan, Shipman and Sinha²⁷. They concluded that in the presence of cylinder at the upstream edge of the cavity, the oncoming flow was obstructed and deflected upwards, thereby impairing the efficiency of its interaction with aft wall necessary for the cavity tone generation.

The hypothesis of high frequency forcing as an agency behind the cavity tone suppression has its roots in the work of Wiltse and Glezer²⁸. They found a dramatic alteration in the development of a turbulent shear layer upon perturbing it at very high frequency. They showed that exciting the shear layer in its transitional region at a frequency three to four times higher than its natural unstable frequency, resulted in dramatic increase in the turbulence dissipation rates. Numerical simulations of Cain *et al.*^{29,30} showed that in addition to an increase in the turbulence dissipation rates, there was also a reduction in the turbulence production rates associated with high frequency excitation. Stanek *et al.*³¹ argued that vortices shed by the cylinder at very high frequency may provide the necessary perturbations to the shear layer developing over the cavity to constitute the case of high frequency forcing. The high frequency forcing, in the form of vortex shedding, is considered to interfere with the development of the instability waves within the shear layer; and consequently with the mechanism of cavity tone generation.

The wake behind the cylinder changes the mean velocity profile of the shear layer. It has been argued that the time averaged shear layer profiles downstream of the cylinder in crossflow configuration are more stable compared to the mixing layer profiles observed for a baseline configuration with no control. Thus, the cavity tone suppression due to the cylinder could be attributed to the modification of the shear layer velocity profile and its stability characteristics.

C. Methodology of Current Work

In the present study we intend to investigate the working principle of the rod in cross flow actuator, with the focus on evaluating the stability hypothesis using experimental data and theoretical calculations. The current paper begins with a description of the experimental facilities and instrumentation used in our study. This is followed by a section which introduces the spatial linear stability problem for two-dimensional, locally parallel, compressible, inviscid flows. In this section we discuss the nature of the mean velocity profiles for the classical shear layer flow as well as the modified flow downstream of the cylinder in crossflow configuration. For this latter configuration, the modified mean velocity profiles downstream of the cylinder are referred to as the ‘hybrid profiles’ and contain five adjustable parameters that can be suitably varied in order to best fit the experimentally measured mean velocity profiles. The discussion section which follows is divided into four subsections. In the first subsection, we present results and discuss the acoustic data acquired for the baseline flow (i.e. flow without any control technique) and the control flow (obtained by placing the cylinder at several different locations). Next, the stability characteristics of the hybrid velocity profile are discussed with regard to the number of unstable modes as well as the changes in these instability characteristics with change to the profile parameters. This is done by creating synthetic profiles by changing the various parameters and studying the corresponding changes in the stability characteristics (instability growth rate and phase velocities). Following this, we turn our attention to the stability characteristics of the experimentally measured mean velocity profiles. In this regard we first present mean velocity profiles measured downstream of the cylinder in crossflow. These profiles were measured by changing the transverse and streamwise location of the cylinder. Finally, we discuss the relevance of our stability results when examined in the light of the resonance suppression benefits of the cylinder in crossflow configuration.

III. EXPERIMENTAL FACILITIES AND INSTRUMENTATION

The present set of experiments were conducted at the High Speed Flow Facility in the Fluid Dynamics Research Center of the Illinois Institute of Technology. Compressed air passes through a plenum before exiting into the ambient from a rectangular slot nozzle

having dimensions 10.17 mm. \times 50.80 mm. (0.4 in. \times 2.0 in.). The interior of the nozzle has an elliptical contour in order to ensure smooth flow at the exit. Figure 2 shows a schematic of the experimental setup along with the location and orientation of the coordinate axes. An aluminum block containing the cavity ($L/D = 2$) in the form of a rectangular cutout is mounted flush with the bottom edge of the nozzle. The cavity is located equidistant from the transverse edges of the nozzle and has dimensions of length $L = 25.4$ mm, width $W = 25.4$ mm, and depth $D = 12.7$ mm (1.0 in. \times 1.0 in. \times 0.5 in.). The jet flow over the block provides the freestream of air that flows over the cavity. It was verified that the area where the cavity was located lay within the potential core of the jet thereby ensuring a uniform freestream flow over the cavity. For the cavity tone suppression experiments, a cylinder having diameter, $d = 0.794$ mm (1/32 in.), and length of 34.93 mm (1.375 in.) was used. It was secured upstream of the cavity leading edge using two end plates having dimensions 12.57 mm \times 25.4 mm \times 3 mm. Note that we wanted the rod diameter to be small enough to have the shedding frequency of the rod an order of magnitude higher than that of the cavity tone frequency, but at the same time we wanted it to be stiff so that it would not vibrate. Additionally, we wanted the rod to be smaller than or at least equal to the boundary layer thickness. Stanek *et al.*²⁶ examined cylinders of various diameters and found the one with $d = 2/3\delta$, where δ is boundary layer thickness, to be the most effective. Keeping in mind all these design criteria, we found 0.794 mm (1/32 in., which is a standard available size) to be a suitable choice. Experiments were performed for cylinders placed at several different locations in the X and Y direction to investigate the effect of cylinder on the stability and the cavity tone suppression. Various control configurations were obtained by changing the gap, g , which is the distance between the ground and the cylinder centerline, and its axial location in the X direction. Table I gives details of these different locations, along with the nomenclature of the configurations used in the present work. Note that the location where $g/d = 0.50$ corresponds to the case where the cylinder was resting on the ground at the leading edge of the cavity. In order to measure the cavity acoustics, a Brüel & Kjær condenser microphone, flush with the cavity floor, was used. The pressure signal obtained from the microphone was sampled at 200 kHz for 1.024 seconds and band-passed through a 4th order analog Bessel filter.

To measure the boundary layer and shear layer characteristics in the case of the baseline and the various control configurations, a hypodermic pitot probe attached to a Kulite (XCS-

062-25D) transducer was used. The pitot probe had an internal diameter of 0.1016 mm (0.004 in.) and external diameter of 0.2032 mm (0.008 in.). The mean value of the signal measured by the miniature probe at a point was used to calculate the stagnation pressure and subsequently, the axial velocity, at that point. For the current experiments, using the miniature pitot probe, the boundary layer at the upstream edge of the cavity was measured to be 0.8 mm thick at $M = 0.6$. Due to spatial resolution limitations, it was not possible to reliably measure the change in the boundary layer thickness at the other Mach numbers. For this reason, the boundary layer thickness at $M = 0.6$ will be referred to as the nominal boundary layer thickness, δ . Note that the comparison of the experimentally measured boundary layer profiles with the 1/7 power law revealed that the boundary layer was turbulent at all the Mach numbers.

IV. FORMULATION OF THE LINEAR STABILITY PROBLEM

A. The Rayleigh Equation

In an effort to understand the physical mechanism that results in acoustic suppression of cavity flow resonances using the cylinder in crossflow configuration, one of the conjectures that have been put forward is that this configuration alters the mixing layer type mean velocity profile of the baseline configuration to one that is more stable. The stability of compressible, inviscid shear layers have been studied extensively in literature (see, for instance, Lees and Reshotko³² or Michalke^{33,34}).

In order to arrive at the stability equation for an inviscid, compressible flow assuming it to be two-dimensional and locally parallel, we decompose the perturbation pressure, \tilde{p} , as:

$$\tilde{p}(x, y, t) = \hat{p}(y) e^{i(\alpha x + \omega t)}, \quad (2)$$

where \hat{p} is the instability pressure eigenfunction that is dependent on the transverse coordinate alone, α is the streamwise wavenumber and ω is the circular frequency of the instability. Substituting this decomposition into the linearized continuity, momentum and energy equations, we arrive at the compressible Rayleigh equation given by:

$$\frac{d^2 \hat{p}}{dy^2} - \left\{ \frac{2\alpha}{\omega + \alpha \bar{u}} \frac{d\bar{u}}{dy} + \frac{1}{\bar{\rho}} \frac{d\bar{\rho}}{dy} \right\} \frac{d\hat{p}}{dy} - \{ \alpha^2 - M^2 \bar{\rho} (\omega + \alpha \bar{u})^2 \} \hat{p} = 0. \quad (3)$$

In equation (3), terms with an overbar denote time averaged quantities. Equation (3) is the two-dimensional, compressible Rayleigh equation in its nondimensional form. The nondimensionalization has been done as follows: the density ρ and the streamwise velocity, u , have been nondimensionalized using the freestream density and the freestream velocity, ρ_∞ and U_∞ , respectively; the pressure has been nondimensionalized using $\rho_\infty U_\infty^2$; the lengths are nondimensionalized using the cavity depth D ; the streamwise wavenumber, α , has been nondimensionalized using length scale D ; angular frequency, ω , has been nondimensionalized using D/U_∞ . M is free stream Mach number. For a more detailed discussion, in addition to results pertaining to the adjoint equations and the biorthogonality relations, the interested reader is referred to Rowley³⁵.

B. Boundary Conditions

Given the coordinate axes setup as shown in figure 2, and the nondimensionalization scheme, the region of integration extends from $y = -1$ to $y \rightarrow \infty$. Practically speaking, ‘ ∞ ’ is taken to be a large enough number such that the mean flow properties are uniform at this distance. At $y = -1$, we use the wall boundary condition, which is given by:

$$\frac{d\hat{p}}{dy} = 0, \quad \text{at } y = -1. \quad (4)$$

The boundary condition at $y \rightarrow \infty$ requires the pressure \hat{p} to be bounded. Since at $y \rightarrow \infty$, $\bar{u} = \bar{\rho} = 1$, equation (3) breaks down into a simple, constant coefficient second order differential equation. The solution to this equation that is bounded at ∞ is:

$$\hat{p} = Ae^{-\lambda y}, \quad (5)$$

where $\lambda = \sqrt{\alpha^2 - M^2(\omega + \alpha)^2}$. Equations (4) and (5) are the boundary conditions necessary to solve Rayleigh equation given by equation (3).

C. Mean Velocity and Density Profiles

For a shear flow between two fluids that have the same velocity magnitude and opposite direction, the mean velocity profile has traditionally been described using a hyperbolic tangent type equation. For shear flows of the kind pertinent to the cavity flow problem,

given that the velocities of the two fluids are not equal in magnitude, the mean streamwise velocity profile is given by the equation:

$$\bar{u}(y) = \frac{1}{2} \left[1 + \tanh \left\{ \frac{2(y + SL_{off})}{\delta_w} \right\} \right], \quad (6)$$

where δ_w is the vorticity thickness of the shear layer and the term SL_{off} accounts for the transverse offset (if present) of the shear layer. For the cavity tone suppression experiments described in the current paper using a cylinder in crossflow, the velocity deficit induced by the bluff body introduces a wake downstream of the cylinder. The mean velocity for this suppression configuration is a hybrid of the traditional shear layer velocity profile given in equation (6) and a wake profile, and is given by:

$$\bar{u}(y) = \frac{1}{2} \left[1 + \tanh \left\{ \frac{2(y + SL_{off})}{\delta_w} \right\} \right] - W_{amp} \exp \left[- \left\{ \frac{y + W_{off}}{W_{wid}} \right\}^2 \right]. \quad (7)$$

Equation (7) is a combination of the traditional hyperbolic tangent and Gaussian distributions, which simulate the mixing layer and wake parts of the velocity profile respectively, and shall henceforth be referred to as the hybrid profile. In this equation, W_{amp} , W_{off} and W_{wid} represent the wake amplitude, the wake offset and the wake width respectively. Figure 3 shows a sample hybrid velocity profile with the various profile parameters given in equation (7) indicated. A similar expression was used in the work by Koochesfahani and Frierler³⁶ in order to study the stability characteristics of a plane mixing layer which took into account the wake component of the initial velocity profile. This wake component in their work was produced due to the use of a splitter plate to separate the fast and slow moving flows.

The mean density distribution, $\bar{\rho}(y)$ is, in general, dependent on the flow Mach number and its mean velocity and temperature distribution and can be assumed to follow a Crocco relation which was given in Tam and Block²⁰ as:

$$\bar{\rho} = \left[\frac{1}{2} (\gamma - 1) (1 - \bar{u}^2) M^2 + 1 \right]^{-1}. \quad (8)$$

However, for the moderate Mach numbers that are considered in this work, the density distribution has been assumed to be uniform, i.e. $\bar{\rho} = 1$. This was the same assumption that was used in Rowley, Colonius and Basu⁴¹, where flow Mach numbers up to $M = 0.80$ were considered. In the work of Panickar³⁷, it has been shown that at the lower compressible, subsonic Mach numbers, the stability results obtained using either of these mean density distributions are comparable.

Equation (3), subject to boundary conditions (4) and (5) is a differential eigenvalue problem. For spatially developing shear flows, it has been shown in Michalke³⁸ that the spatial formulation of the eigenvalue problem is appropriate and that is the approach we use for this paper. For the spatial stability problem, we look for solutions to (3) that oscillate sinusoidally in time but grow or decay exponentially in space. In mathematical terms, given the normal-mode decomposition in equation (2), this means that for a given $\omega \in \mathbb{R}$ we look for $\alpha \in \mathbb{C}$ where \mathbb{R} and \mathbb{C} are the sets of real numbers and complex numbers respectively. If $\text{Im}(\alpha) < 0$, the solution grows exponentially in space and the eigenvalue and eigenfunction corresponding to such a solution is referred to as an unstable or undamped eigenvalue and eigenfunction respectively. Conversely, if $\text{Im}(\alpha) > 0$, the solution decays spatially and the eigenvalue and eigenfunction corresponding to such a solution is referred to as a stable or damped eigenvalue and eigenfunction respectively. In this paper, we restrict ourselves to finding only the unstable/undamped eigenvalues and eigenfunctions. These unstable eigenvalues are computed using the shooting method.

V. RESULTS AND DISCUSSION

A. Results from Acoustic Studies

Flow over a cavity can produce discrete tones over a very wide range of parameters of cavity dimensions and freestream Mach numbers. However it is not always that these tones are produced by the mechanism based on the acoustic feedback loop explained in §II A. For deep cavities with $L/D < 1$, or for $M < 0.2$, the tones are produced due to normal mode resonance (Tam and Block²⁰). Under certain conditions the cavity flow is prone to an absolute instability - also known as the wake mode (Gharib and Roshko³⁹, Forestier, Jacquin and Geffroy⁴⁰ and Rowley, Colonius and Basu⁴¹). Moreover, even if the tones are produced due to the acoustic feedback loop, external parameters can affect the primary mechanism depending on the experimental configuration. If the freestream flowing over a cavity is obtained by a jet, one could encounter a jet-cavity interaction problem, which is a separate category by itself (Raman, Envia, Bencic⁴²). One simple way to check if the tones obtained in the present experiments are indeed canonical cavity tones is by making sure that the tones follow the staging behavior as characterized by the Rossiter's phase locking

formula given in equation (1).

Figure 4 shows the frequency staging phenomenon associated with the cavity tones along with the theoretical predictions based on the Rossiter formula given in equation (1). The conventional values of κ and ν are 0.58 and 0.3¹⁸. However for the present set of data, $\kappa = 0.75$ and $\nu = 0.30$ are found to give the best fit. The experimental data are in good agreement with the theoretical predictions especially at higher Mach numbers. For a lower Mach number however, the cavity tone frequency seems to drift away from the theoretical predictions. This is in agreement with the work of Tam and Block²⁰, who showed that at these lower Mach numbers, the cavity physics is dominated by normal mode resonance. For the remainder of this subsection we shall present results from experiments where the freestream Mach number $M > 0.5$, and the experimentally measured resonant frequencies agree well with Rossiter's phase locking formula. Thus, we are assured that the cases under study are indeed feedback-reinforced resonant cavity tones.

Figure 5 shows a comparison of the acoustic spectra at $M = 0.6$ for the baseline configuration and two representative control configurations A.2 and A.6. The X -axis is represented nondimensionally in terms of the Strouhal number based on the cavity depth $St_D = \frac{fD}{U_\infty}$; an equivalent dimensional frequency measure (in kHz) is also provided as an alternate abscissa on the top of each spectral plot. The dominant frequency in the baseline spectrum ($f \sim 3.1$ kHz, $St_D \sim 0.20$) agrees well with the theoretically predicted first Rossiter mode. Figure 5(a) shows the spectra over a frequency range up to 30 kHz. In this figure one can clearly see the suppression of the cavity tone spike along with a reduction in broadband acoustic levels achieved by both the control configurations. Broadly speaking, figure 5(a) also shows that the suppression levels achieved by the A.2 configuration are greater than those of the A.6 configuration. Figure 5(b) shows the same spectra for a wider frequency range, up to 80 kHz. The instability frequency corresponding to the coherent spanwise vortices shedding from the cylindrical rods are seen in this figure at approximately 48 kHz (Strouhal number based on cylinder diameter, $St_d \sim 0.17$). For the size of the cylinder and range of the Mach numbers we are working with, the operational range (Reynolds number based on the cylinder diameter, $Re_d < 10^4$) of the cylinder is well below the critical transition regime. In this regime, it is well known that the frequency of the periodic shedding from the cylinder remains approximately constant at $St_d \sim 0.2$. The spectra in figure 5(b) show the spectra of the control configurations can be demarcated into two regimes. The first regime is the

low frequency regime where the acoustic levels of the control configurations are lower than those in the baseline configuration. The second regime is the mid to high frequency regime where the acoustic levels in the control configuration are comparable to, or as shown for the spectra of the A.6 configuration, higher than, those in the baseline configuration. However, it should also be noted that the vortex shedding occurs at a frequency that is more than one order of magnitude higher than the frequency of the most dominant instability in the baseline configuration, i.e. the first Rossiter mode.

Figure 6 shows the acoustic characteristics of the baseline configuration. The very high tonal SPL values in this figure are indicative of the strong feedback enhanced acoustic resonance mechanism present in this baseline configuration. To measure the efficacy of the cavity tone suppression device one of the most commonly used metrics is the overall sound pressure level (OASPL). However in the present work, although the cylinder in cross flow configurations suppress the cavity resonant tones, they add self noise at frequencies corresponding to $St_d \sim 0.17$ (the periodic vortex shedding frequency). This corresponds to frequencies of approximately 40-70 kHz depending on the Mach number of the flow. For this reason, the OASPL is not suitable for the present study since it is independent of the frequency range. In order to evaluate the effect of the cylinder in crossflow configurations on the cavity tones from a scientific standpoint, one must exclude the self noise of these configurations from the cavity tones. Hence we introduce a metric, SPL_{20kHz} , which we define as:

$$SPL_{20kHz} = 20 \log \left[\frac{\sqrt{\sum_{100 \text{ Hz}}^{20 \text{ kHz}} p^2}}{p_{ref}} \right] \quad (9)$$

where $p_{ref} = 20\mu\text{Pa}$. As can be seen in figure 6, the difference between SPL_{20kHz} and the OASPL for the baseline configuration is marginal (< 0.3 dB), which reinforces the conjecture that the majority of the cavity flow acoustics for this configuration are mainly concentrated at frequencies below 20 kHz. It is also found that even though changing the Mach number changes the frequency of the cavity tones (see figure 4), the SPL_{20kHz} value does not change considerably and remains within the narrow band of 156 to 158 dB.

Figure 7 shows results for the cavity tone suppression as a function of the gap, g/δ , and the Mach number, M , where, as mentioned earlier, δ is the nominal boundary layer

thickness. The data presented in figure 7 have been acquired at finer increments of the gap g than tabulated in table I. This is done in order to better determine the optimal cylinder location from the point of view of acoustic suppression. The Y -axis is represented as the change in the SPL_{20kHz} metric between the baseline configuration and the control configuration under consideration, with positive values of ΔSPL_{20kHz} indicating an acoustic suppression by the control configuration. Figure 7(a) shows results for the cylinder placed at $x/d = -1.59$ (cylinder location ‘A.×’ in table I), whereas figure 7(b) corresponds to the cylinder placed at $x/d = -6.35$ (cylinder location ‘B.×’ in table I) from the cavity leading edge ($\times=1, 2, \dots, 6$). In both figures 7(a) and 7(b), at all the Mach numbers, the suppression characteristics show a similar trend with respect to changing the gap g/δ . Starting with the cylinder location having the largest g/δ , it is seen that reducing the gap between the cylinder and the ground, at a given Mach number, increases the efficacy of the control configuration in suppressing acoustics of the baseline configuration. This trend continues until it reaches a maximum after which any further decrease in the gap reduces the suppression provided by the control configuration at that particular Mach number. It is seen that at $g/\delta = 0.5$, i.e. when the cylinder is resting on the ground, the acoustic suppression provided by the control configuration at a particular Mach number is markedly lower than when there is gap between the cylinder and the ground. Figure 7 also indicates that as the Mach number is increased, the efficacy of the cylinder in suppressing the cavity tones deteriorates. Finally, it can be concluded that for a majority of the cases, moving the cylinder upstream reduces the efficacy of the cylinder in suppressing the cavity tones.

As far as the optimum location of the cylinder is concerned, one of the pertinent questions is, which parameter is more sensitive for cavity tone suppression: moving the cylinder upstream or raising the cylinder above the ground? A comparison between figure 7(a) and (b) shows that raising the cylinder above the ground is more sensitive in suppressing the cavity tones. For example consider the $M = 0.5$ case at $g/\delta = 1.14$. Moving the cylinder upstream by approximately 5 equivalent cylinder diameters ($5d$) in the X direction reduces suppression by approximately 1 dB. However moving the cylinder in the transverse (Y) direction by $\sim 5d$ reduces the suppression by more than 5 dB. As far as the optimum location in the Y direction is concerned, Ukeiley *et al.*²³ suggest that the cylinder should as high as possible, yet completely contained within the boundary layer. Stanek *et al.*²⁶ claim that the optimum gap between the cylinder and the ground should be 2/3rd of the boundary

layer thickness, which corresponds to $g/\delta = 1.16$ for the current experiments. In the present study we found the optimum gap g/δ to be 1.14. Since, each of these studies pertain to a different cylinder diameter, further work needs to be done with different cylinder diameters to find more accurate and universal optimum Y location.

B. Stability Characteristics of the Synthetic Profile

As mentioned in §II C, one of the goals of the present study is to investigate the stability characteristics of the experimentally measured velocity profiles as the cylinder location is varied in the X and Y direction. However, as opposed to the stability characteristics of the classical shear layer velocity profile given in equation (6) the stability characteristics of the hybrid profile given in equation (7) have not been studied extensively. Rather than constructing a hybrid mean velocity profile with arbitrary values of the profile parameters, we selected the mean profile corresponding to the control configuration A.5 and using equation (7) fitted a curve to this profile in order to arrive at optimal values of the profile parameters SL_{off} , δ_w , W_{amp} , W_{off} , and W_{wid} . Similarly, equation (6) was used to fit a curve to the experimentally measured mean velocity profile of the baseline configuration and arrive at optimal values of SL_{off} and δ_w for this configuration. These profiles, obtained by fitting theoretical curves to experimental data, are referred to as the *principal profiles*. Note that the choice A.5 case is not motivated from its acoustic suppression characteristics; it is chosen because the velocity profile of A.5 case was easy to modify-due to its symmetrical and clearly discernible wake. The stability characteristics of these principal profiles were obtained by solving the spatial eigenvalue problem given by (3) for various values of the frequency ω , using the shooting method. This method requires a starting guess for α in order to initiate an iterative solver (the Newton-Raphson method) which, in turn, provides an optimal value of the eigenvalue α . In the case of the principal profile corresponding to the baseline configuration, the eigenvalue for the starting guess was obtained using a vortex-sheet model at the given Mach number. Since a vortex-sheet model corresponding to the hybrid profile was not available, the eigenvalue for the principal profile corresponding to the A.5 configuration was obtained using a trial-and-error method. Once the unstable modes of the principal profiles were obtained, we then parametrically varied the shape of these principal profiles to produce various *synthetic profiles*. The instability modes of these synthetic profiles

were obtained using the solutions of the principal profiles as the initial guess. All the stability calculations were performed for a freestream Mach number of $M = 0.6$.

1. *Existence of Multiple Instability Modes*

The unbounded free shear flow described by a tanh type curve is known to have only one instability mode (Rowley³⁵). However, when simulated experimentally, the mean velocity comprises of the wake of the splitter plate wake superimposed on the shear layer, typical of the the hybrid profile given in equation (7). Koochesfahani and Frieler³⁶ studied the stability of such profiles. They showed the existence of two modes, which they termed as the shear layer mode and the wake mode, for such hybrid profiles. The shear layer mode had a larger instability growth rate and it's eigenfunction had a single peak that was aligned with the midpoint of the shear layer. The wake mode had two peaks placed across the wake part of the hybrid profile. The streakline pattern revealed that the shear layer mode was sinuous whereas wake mode was varicose in nature. Here, it must be noted that the wake mode described in the Koochesfahani and Frieler³⁶ is different from the wake mode described in the work of Gharib and Roshko³⁹, Rowley, Colonius and Basu⁴¹ and Forestier, Jacquin and Geffroy⁴⁰.

Although the velocity profiles in the present study have the same hybrid form, they differ in their boundary condition, i.e., the velocity profiles in the studies of Koochesfahani and Frieler are unbounded, whereas in the present case they are bounded on one side by the cavity floor. Here, the discussion regarding the existence of multiple unstable modes is relevant because the shooting method provides only one solution at a time. In the current work, this issue is addressed with the help of principal profile A.5 and its synthetic variants. Changing the initial guess by a trial-and-error method, we were able to find two unstable modes for the principal profile corresponding to this configuration. Figure 8(a) shows the experimentally measured mean velocities (shown using open symbols) for configuration A.5 along with the best fitting curve for this configuration (indicated by the solid curve) obtained using equation (7). The empirical parameters that describe the shear layer and wake parts of the hybrid mean velocity profile are also shown in this figure. Two sample eigenfunctions corresponding to the two unstable modes obtained for this principal profile are shown in figures 8(b) and (c). These eigenfunctions have been normalized by the maximum amplitude of the pressure

eigenfunction in the domain. As seen from the figures, out of the two unstable modes, one mode has a double lobed peak aligned with the wake part of the profile. We refer to this unstable mode as eigenmode ‘I’ (8(b)). The other unstable mode, has its peak aligned with the shear layer part of the profile. This unstable mode will be referred to as eigenmode ‘II’ (8(c)).

2. Phase Velocities and Growth Rates of Synthetic Profiles

We begin by studying the effect of changing the wake amplitude parameter, W_{amp} , in equation (7). Figure 9(a) shows a few sample synthetic variants (obtained by varying parameter W_{amp}) of the principal profile corresponding to the control configuration A.5. These synthetic variants can be experimentally obtained as one moves downstream along a wake; the further downstream one goes, the lower the value of W_{amp} obtained (although, in practice, the reduction in wake amplitude as one moves further downstream along a wake is accompanied by a larger wake width in accordance with the law of conservation of momentum; additionally, for our configurations, the presence of a ground adjacent to the wake on one side adds to the complexity of the flowfield). As far as the growth rates of the two unstable modes is concerned, it is observed that as the velocity deficit in the wake reduces, i.e. as W_{amp} decreases, the instability growth rate of eigenmode I keeps decreasing as shown in figure 9(b). This behavior is expected since it can be seen from equations (7) and (6) that when $W_{amp} = 0$, the hybrid velocity profile reverts back to being a classical shear layer profile. Since the classical shear layer profile has only one unstable mode it makes sense that eigenmode I would cease to exist when the wake is eliminated. As far as the phase velocities for this mode are concerned, it is seen from figure 9(b) that the phase velocities increase marginally as the wake amplitude is reduced, although for a given value of W_{amp} , the phase velocities remain approximately constant over almost the entire frequency range. In contrast to the behavior for eigenmode I it is seen that the growth rates for eigenmode II remain fairly unchanged as W_{amp} is varied, as shown in figure 9(c). This is to be expected since eigenmode II is dependent on the shear layer characteristics rather than the wake characteristics. The phase velocities for this eigenmode initially increase with an increase in the instability frequency before reducing and remaining constant at approximately half the freestream velocities ($U_c = 0.5U_\infty$) for the higher instability frequencies. Comparison

between figures 9(b) and (c) also show that growth rates of eigenmode II are substantially higher than that of the eigenmode I.

Next, we create synthetic profiles by changing the values of the wake width parameter, W_{wid} , in equation (7). Some sample profiles illustrating this behavior are shown in figure 10(a). Such mean profiles could be experimentally generated by using cylinders of different diameters. The instability growth rates for modes I and II for these profiles are shown in figures 10(b) and (c) respectively. It can be seen from figure 10(b) that as the wake becomes wider, i.e. as W_{wid} increases, the frequency range and the maximum amplitude of the instability growth rate for mode I reduces. On the other hand, the instability growth rates for mode II remain unchanged. This figure shows that as W_{wid} becomes narrower, for all other parameters remaining the same, the growth rate of mode I becomes greater than that of mode II. For mode I, as seen from figure 10(b), the phase velocities at a given value of W_{wid} increase as the frequency increases. Additionally, as W_{wid} increases, the phase velocity at a given frequency is greater for a configuration with a wider wake. In the case of mode II, for various values of W_{wid} , the phase velocities are identical at higher frequencies. At lower frequencies, the phase velocity decreases as W_{wid} decreases.

Changing the wake offset parameter, W_{off} physically moves the wake towards or away from the shear layer. Synthetic profiles indicating this behavior are shown in figure 11(a). Mean profiles of this kind can be experimentally generated by changing the gap, g , between the cylinder and the cavity. The instability growth rates for modes I and II for the profiles shown in figure 11(a) are shown in figures 11(b) and (c) respectively. It is seen that the growth rate of the instability mode I is unchanged as long as the value of W_{off} is such that the wake and the shear layer remain separate. However, once this condition is no longer valid, it can be seen that the more velocity deficit of the wake lies within the shear layer, the smaller the maximum amplitude of the growth rate of, and the smaller the range of, the instability frequencies corresponding to instability mode I. Similar results are seen in the case of instability mode II (figure 11(e)) wherein the growth rates for this mode remain unchanged as long as the wake and the shear layer remain separate. It is seen that as the values of W_{off} are systematically reduced, it becomes difficult to obtain two distinct instability modes; refer to the curve corresponding to $W_{off} = 0.10$ where stability results are only obtained for mode II. Thus, merging the wake and the shear layer leads to a merging of the growth rate characteristics of modes I and II. The phase velocities for both modes

are observed to be close to half the freestream velocity at higher frequencies. At lower frequencies, it is seen that the phase velocities of mode II are higher than those of mode I.

The effect of changing the vorticity thickness of a classical tanh-type shear layer profile given by equation (6) is well known. These results, which may be found in the references cited in the beginning of §IV, can be summarized as follows:

1. Starting with the vortex-sheet model ($\delta_w = 0$) which is unstable at all frequencies, increasing the vorticity thickness causes the shear layer to be unstable to a finite range of frequencies. This frequency range reduces as the vorticity thickness is increased.
2. As the Mach number increases, the maximum growth rate keeps reducing until at a high enough Mach number the shear layer is no longer spatially unstable at any frequency.

Figure 12 shows the effect of changing the vorticity thickness (δ_w) of the classical tanh-type shear layer profile, on the growth rates of the first two Rossiter modes at $St = 0.19$ and $St = 0.4$. It is seen that, for both first and second Rossiter modes, increasing δ_w first increases the growth rates, until they achieve a maximum value, following which any further increase in δ_w leads to a reduction in the growth rate of these two Rossiter modes. Here compared to the first mode, the second Rossiter mode shows fast variation, especially with respect to the drop in the growth rate at higher values of δ_w . For small δ_w values, the growth rate of second Rossiter mode is higher than first; this trend reverses for $\delta_w > 0.24$.

For the hybrid profile, figure 13(a) shows mean profiles obtained by changing the vorticity thickness parameter, δ_w , in equation (7). Figures 13(b) and (c) show the instability growth rates of modes I and II respectively. Here it is seen that the growth rates of the instability mode I remain largely unchanged as the vorticity thickness is changed (figure 13(b)). On the other hand, as shown in figure 13(c), the growth rates of instability mode II changes in a manner that is consistent to the changes that occur in classical shear layer type profiles. For mode I, as shown in figure 13(b), the phase velocities are identical for the entire frequency range for all values of δ_w . As far as mode II is concerned, for a given value of δ_w , the phase velocities at the higher frequencies are remain fairly constant. At the lower frequencies, the phase velocities are higher for lower values of the vorticity thickness. Both, modes I and II, have nearly identical phase velocities (half the freestream velocity) at the higher frequencies.

The stability characteristics of synthetic profiles obtained by changing the value of the SL_{off} parameter are similar to the ones obtained by changing the W_{off} parameter. This is because a change in either of these parameters leads to a change in the physical location of the wake with respect to the shear layer. Hence, in the interest of brevity, the characteristics of the profiles obtained by changing SL_{off} have not been separately discussed. Similarly, if both SL_{off} and W_{off} are simultaneously changed such that the resultant mean velocity profile is a linear translation of the original profile, the stability characteristics of this resultant profile, for, both, modes I and II, are identical to the original profile.

The stability calculations indicate that as long as the velocity defect due to the wake is physically located such that it does not interact with the shear layer, instability modes I and II are distinct and the growth rates and phase velocities of both these modes can be obtained. As the wake starts merging into the shear layer, the growth rates of both instability modes I and II become comparable. Hybrid mean velocity profiles where the wake and shear layer parts of the profiles are merged to some extent can be experimentally obtained for cylinder locations having smaller gaps; this will be shown in greater detail in the §V C. For configurations where the velocity deficit due to the wake is merged with the shear layer to a much larger extent, it becomes difficult to distinguish two separate modes I and II as was shown in figure 11. It was found that as long as the wake and shear layer parts of a given hybrid profile were physically separate, mode I was sensitive to the changes in the wake, but insensitive to the changes in the mixing layer; conversely, mode II was sensitive to the changes in the shear layer, but insensitive to the changes in the wake.

C. Study of Experimentally Measured Velocity Profiles

1. Mean Velocity Measurements

We now turn our attention to the results obtained by mean velocity measurement experiments for the baseline and control configurations. Figure 14 shows mean velocity profiles measured at the spanwise center of the cavity ($z = 0$) at a streamwise location, $x = 0.08$, for the baseline and control configurations. The streamwise location is sufficiently close to the upstream edge of the cavity that the profiles measured at this location, when used for spatial linear stability calculations, would provide reliable measures of growth rates of the

instabilities affecting the cavity flow physics. The mean velocities measured for the control configurations listed in table I, as well as for the baseline configuration, are shown by open faced symbols in figures 14(a) and (b). The solid lines in these figures are the curve fits to the measured velocity profiles obtained by using equations (6) or (7), as applicable. Starting with the profile shown at the bottom, which corresponds to the baseline configuration, each successive profile is shifted by one unit on the Y-axis in order to facilitate ease of viewing.

When the cylinder is located on the ground upstream of the cavity (configurations A.1 and B.1), the mean velocity measurements are once again well predicted using a hyperbolic tangent type equation given by (6), similar to that for the baseline configuration. The principal difference between the mean velocity profile curve fits for configurations A.1 and B.1 versus the baseline configuration is that the shear layer offset parameter, SL_{off} , is much larger in the case of the former configurations as compared to the latter configuration. This indicates that placing the cylinder on the ground not only inhibits the formation of a wake, but also results in a transverse deflection of the shear layer above the cavity, which nevertheless develops in accordance with the classical hyperbolic tangent type equation given by (6). As we move progressively upwards, along the Y-axis of figures 14(a) and (b), from the profile for configuration A.2 (or B.2), the location of the wake is seen to translate in the transverse direction. This is an indication of the progressively larger gap between the cylinder and the ground for each subsequent configuration. For smaller gaps between the cylinder and the ground (configurations A.3, A.4, B.3 and B.4), the wake is seen to be asymmetric. This is due to the fact that for these configurations some portion of the cylinder is located within, or very close to, the boundary layer upstream of the cavity leading to unequal velocities above and below the cylinder. This asymmetry is not seen for configurations having larger gaps (A.5, A.6, B.5 and B.6). Finally, it is seen that the mean velocity profiles corresponding to cylinder locations further away from the upstream edge of the cavity (figure 14(b)) have more diffused wakes than those corresponding to cylinder locations closer to the upstream edge of the cavity (figure 14(a)). When expressed in terms of the parameters given in equation (7), this means that the magnitude of the parameter W_{amp} is greater for the ‘A.x’ configurations than those for the corresponding ‘B.x’ configurations.

Figure 15 shows the mean velocity profiles at various streamwise locations for the baseline and control configurations. These measurements were taken along the spanwise center of the cavity ($z = 0$). As one moves downstream, the shear layer becomes thicker and the wake

starts diffusing. As expected, the baseline and A.1 configurations do not show the presence of a wake at any of the streamwise locations. For configuration A.2 it is seen that the wake completely merges with the shear layer within a short distance from the leading edge of the cavity; in contrast, for configurations A.4 and A.6, the signature of the wake is observed for a larger streamwise distance. The uncertainty analysis of one of the velocity profiles, i.e., Baseline velocity profile measured at $x = 0.72$, showed that the data that lay outside of the cavity is highly consistent, i.e., the errors are less than 2%. The repeatability of the data reduces as one moves inside of the cavity, although the error never exceeds 10%.^{1,11} Note that for the case A.6, when the wake is out of the influence of the shear layer, the development of the wake in terms of its decay rate etc., closely follow the classical turbulence theory⁴³. This suggests that at a sufficient distance away from the shear layer the wake develops as a separate entity. In conjunction with the results presented in figure 12, one can argue that merging of the wake with the mixing layer can make the shear layer thick enough so that at some point even the Rossiter modes cannot be amplified. In that case it is not the growth rate at one location but the integrated growth rate that would determine the amplification of a disturbance at the upstream edge of the cavity. These integrated growth rates are calculated in the following section.

2. *Stability Results for the Measured Profiles*

We now present results from our investigation of the stability characteristics of the experimentally measured mean velocity profiles shown in figures 14. Figure 16(a) and (b) show the growth rates for instability modes I and II respectively for cylinder locations close to the upstream edge of the cavity (locations 'A.×' in table I). Note that for configurations A.1 and A.2, the wake is either nonexistent or is merged with the shear layer to such an extent that only instability mode II exists. For mode I, figure 16(a) indicates that configurations with large enough gap, such that the only effect of changing the cylinder location is to shift the location of the velocity deficit of the wake in the Y direction (configurations A.5 and A.6), have similar growth rates. For these configurations, the amplitudes of the velocity deficit region of the wake were similar, as was shown in figure 14(a). On the other hand, the growth rates of mode I for configurations A.3 and A.4, where the velocity deficit produces wakes having smaller amplitudes, are much smaller than for configurations A.5 and A.6.

For mode II, figure 16(b) shows that as the gap between the cylinder and the ground is increased, the growth rates for the configurations A.5 and A.6 become increasingly similar to that of the baseline configuration. This is to be expected since a larger gap will allow for the flow underneath the cylinder to develop similar to the baseline as though the flow did not sense the presence of the cylinder. For configurations A.3 and A.4 the interaction of the cylinder with the boundary layer upstream of the cavity results in a pseudo-thickening of the shear layer; the growth rates of mode II for these configurations are indicative of the result of this thickening of the shear layer. For configuration A.2 the gap is even smaller and the wake is barely discernible downstream of the cylinder; this results in the formation of the thickest shear layer (amongst all the 'A.×' configurations) at the measurement location and, consequently the lowest maximum growth rate. For configuration A.2, the lofting of the shear layer results in the formation of a slightly thinner shear layer (as compared to the baseline configuration) at the measurement location. This is reflected in the growth rate characteristics for this configuration (range of instability frequencies and maximum growth rate being slightly larger than the baseline configuration).

For cylinder locations upstream of the leading edge of the cavity (locations 'B.×' in table I), the growth rates of instability modes I and II for the experimentally measured profiles are shown in figure 17(a) and (b) respectively. Once again, only instability mode II is shown for configurations B.1 and B.2. As explained in reference to figure 14(b), the location of the cylinder allows for a greater development of the wake; this is indicated by mean velocity profile measurements which show a more diffuse wake that has a smaller amplitude and larger width. As indicated in §VB, a reduction in the the wake amplitude results in the reduction in the maximum growth rate for mode I. This can be seen by comparing the growth rates for configurations B.5 and B.6 (in figure 17(a) to those for configurations A.5 and A.6 (in figure 16(a)); as expected, the growth rates for the former are much smaller than those for the latter. As the cylinder is brought closer to the ground, the wake region begins merging with the shear layer region leading to the production of wakes having smaller amplitudes, as seen for configurations B.3 and B.4. Hence, for these configurations, in figure 17(a), trends that are consistent with configurations A.3 and A.4 (where a similar merging of the two regions occurred), are observed; the configurations closer to the ground (B.3 and A.3) have smaller maximum growth rates and range of instability frequencies compared to the configurations further away (B.4 and A.4). For instability mode II, figure 17(b) shows

that when the cylinder is placed on the ground, it acts as a boundary layer trip, thickening the boundary layer compared to the baseline configuration, and leading to a correspondingly thicker shear layer downstream of the leading edge of the cavity. For this reason, the growth rate for configuration B.1 has a much smaller growth rate and instability frequency range compared to the baseline. As the cylinder is moved in the transverse flow direction, the flow underneath it tends towards that of the baseline which is indicated by the growth rate of mode II getting closer to the baseline for configurations B.5 and B.6. For configurations B.3 and B.4, the merging of the wake and shear layer regions leads to a perceived increase in the vorticity thickness of the shear layer. This results in the growth rates of mode II for these configurations being smaller than that of the baseline as well as the B.5 and B.6 configuration, although not as small as the B.1 configuration. For configuration B.2, where the wake and shear layer regions are merged to a large extent, the maximum growth rate amplitude is similar to the baseline; however this configuration also has the smallest range of instability frequencies.

To get an insight into the trends of instability mode II, we focus on the relation between the vorticity thickness, δ_w , of the mixing layer part of the profile and maximum growth rate for a given value of δ_w . This relation is shown in figure 18 for the synthetic profiles and for the experimentally measured profiles. This figure also shows the variation of the maximum growth rate of synthetic variants of the baseline profiles as a function of δ_w . It is seen that the maximum growth rate is inversely proportional to the vorticity thickness. One can also see that growth rate is especially sensitive at smaller values of δ_w ; for large values of parameter δ_w , there is very little variation in the maximum growth rate. The data for the experimentally measured profiles is in agreement with the trend for the synthetic profiles. Thus, comparing stability envelopes of mode II in figures 16(b) and 17(b), and the trend for the maximum growth rate in figure 18, it can be concluded that the vorticity thickness of the shear layer part of the hybrid profile dictates the stability of mode II of the experimentally measured profiles, independent of the presence of the wake. A similar conclusion cannot be drawn with respect to mode I since the stability of this mode is affected by changes to both, the wake amplitude as well as the wake width.

Now we turn our attention to the integrated growth rates for the experimental velocity profiles. The amplitude of a given instability mode is calculated by integrating the complex growth rate α_i over the streamwise locations. For the pressure eigenfunctions calculated in

the current study, this is given as:

$$\tilde{p}(x, y) = \hat{p}(y) \exp\left(i \int_0^x \alpha dx\right). \quad (10)$$

where in accordance with our parallel flow assumption, α is supposed to be constant. However, as seen from the streamwise velocity profile measurements in figure 15, the experimental flowfield is slowly diverging. This means that both, α as well as the eigenfunction \hat{p} are actually slowly varying functions of the streamwise position x . Figure 19 shows the integrated growth rates for the configurations shown in figure 15, i.e., baseline, A.1, A.2, A.4 and A.6 profiles. These growth rates are based on numerical integration of the expression in equation (10) along the streamwise direction. For cases A.4 and A.6, results for both mode I and mode II are shown. For rest of the cases, due to the absence of discernible wake, only stability mode II could be obtained. Figure 19(a) shows the growth of the first Rossiter mode, whereas figure 19(b) shows growth of the second Rossiter mode. For both Rossiter modes, the growth rate of the mode II is higher than that of mode I. Downstream of the $x = 0.25$, the difference between the stability mode I and II is almost 100%, which is not surprising knowing the results of the stability mode I and II in relation to the study of the synthetic profiles. For all the configurations except A.4, the growth rate of the first Rossiter mode is the same throughout the cavity length. For control case A.4 the growth rates are higher, especially at downstream locations of the cavity. For the second Rossiter tone, there seems to be no particular trend. For the baseline case downstream of $x = 0.32$, the second Rossiter mode is not amplified. Control cases A.1, A.2 and A.4 show consistently higher growth when compared to baseline cases, whereas A.6 shows the least growth.

D. Relevance to Cavity Resonance Suppression

As mentioned in the §II B, it has been suggested that the acoustic suppression benefits provided by a cylinder in crossflow configuration are a result of enhanced stability characteristics of its modified mean velocity profile. To this end, the primary objective of this paper was to develop the spatial linear stability theory based on this modified mean velocity profile and understand its role in the cavity resonance suppression benefits. In the present study the frequency of the most amplified Rossiter tone, from our experimental data, is found to be 3.1 kHz at $M = 0.6$. This is equivalent to a Strouhal number (based on the cavity

depth D), $St_D = 0.20$. Compared to this, the maximum frequency that can be amplified in the baseline flow is typically 5 to 6 times the Rossiter frequency (refer to the stability curve for the baseline configuration in figure 16(b)). For all the cylinder locations tested, the baseline cavity Rossiter mode frequency always lies within the range of unstable frequencies. As far as the acoustic suppression characteristics are concerned, it is seen that the A.2 configuration shows the maximum suppression in the sound pressure levels, compared to the baseline, at all the Mach numbers. For this configuration, as shown in figure 16, only the mode II instability could be detected. The maximum growth rate for this mode was calculated to be much lower than the maximum growth rate of the baseline configuration. This would indicate that if enhanced stability is the driving force behind cavity resonance suppression achieved using the cylinder in crossflow configuration, it is manifested in the form of a reduced amplitude of the maximum growth rate. However, it can also be argued that since the most amplified frequency in the baseline configuration is the Rossiter mode at $St_D = 0.20$, then for the stability hypothesis to have some bearing on the cavity tone suppression, one would expect to see a change in the growth rate at this particular cavity resonance frequency. At this point we would like to introduce the notion of the cavity as a control system. According to Rowley *et al.*⁴⁴ resonating cavity does not necessarily always have to be an unstable system, wherein the shear layer growth rate is saturated due to the non-linear limit cycle processes. They showed that under certain conditions the cavity can behave as a weakly damped linear system, wherein the integrated growth of the shear layer is proportional to its initial perturbation. For the foregoing linear stability analysis of the shear layer to be valid it is imperative that when controlled the cavity shear layer does not saturate. This would imply that cases with large suppression would exhibit smaller integrated growth, and cases with small suppression would exhibit comparatively higher growth at the Rossiter tone frequency. Contrary to our expectation one sees very little or no correlation between the growth rates and the suppression data. This is because, as shown in figure 16(b), in the Strouhal number range up to $St_D \sim 0.5$ the growth rates for all the control configurations differ only marginally from those of the baseline configuration. Calculations of the integrated growth rates reveal that the baseline configuration and the configuration showing the best suppression characteristics (A.2) have comparable instability magnitudes for instability mode I. This is true for both, the first as well as second Rossiter modes.

In present problem, apart from the shear layer stabilization, effects such as high frequency

foreing and shear layer lift off are also present. The work of Sarpotdar and Raman⁴⁵ and Bastrzyk and Raman⁴⁶) investigated the issue of shear layer lift off in a great detail. They fitted equation 7 to a number of experimentally measured velocity profiles for different control cases to characterize the shear layer lift off in terms of the parameter SL_{off} . They found that the cases with higher acoustic suppression tended to have higher values SL_{off} . Their work also showed that increased shear layer lift off was assoeiated with the reduced impingement of the shear layer onto the trailing edge of the cavity. Since the impingement of the shear layer can generate turbulence length scales across the whole spectrum, the lift off effect, and consequently the reduced impingement of the shear layer, could explain the ability of the rod to reduce the broad band noise levels (see Fig.5). However, their results could not explain all the suppression trends reported in the present work, e.g., they were unable to comment on the optimum gap between the cylinder and the ground. This suggests that multiple mechanisms might be play concurrently in suppressing the cavity tones.

VI. CONCLUSIONS

As an actuator that provides cavity resonance suppression, the cylinder in crossflow technique holds promise. However, it is necessary to understand the physics governing this resonance suppression mechanism in order to optimize actuator design for achieving maximum suppression performance. In the current paper, a detailed parametric study was undertaken, with regards to actuator location, in order to better understand its suppression characteristics. A thorough examination of our acoustic data revealed the following interesting points:

Starting from a gap, $g = 4.5d$ (cylinder located in the freestream), reducing the gap is found to enhance its suppression performance until an optimum gap is reached. Any further reduction in the gap past this optimum leads to a deterioration in the suppression performance. In the present study the optimum gap is found to be $g/\delta = 1.14$ or $g/d = 1.15$. For the current study, it is found that the suppression characteristics of the cylinder in crossflow configuration deteriorate as the freestream Mach number is increased. Finally, moving the cylinder upstream also reduces the efficacy of the cylinder in suppressing the cavity tones.

In order to understand the mechanism of resonance suppression by the cylinder in cross-

flow configuration, we studied the linear stability characteristics of the modified mean velocity profile of this configuration. To this end, we developed the spatial, linear stability theory for nearly parallel, inviscid, compressible shear flows incorporating the modified mean velocity profile relevant to this analysis. The equation for this modified mean velocity profile, referred to as the hybrid profile since it is a combination of the classical shear layer profile and a wake profile, contains five parameters that were individually varied in order to understand the effect of each parameter on the stability characteristics. Following this, we examined the instability growth rates of experimentally measured mean velocity profiles in an attempt to correlate them to our acoustic suppression results. The following interesting results emerged from the stability analysis:

The hybrid profile has at least two unstable modes; these two modes are referred to as mode I and mode II (which correspond to the wake mode and shear layer mode respectively in the Koochesfahani and Frielcr³⁶ study). Reducing the wake amplitude (i.e. the velocity deficit associated with the wake) reduces the maximum growth rates of instability mode I. As the wake disappears from the velocity profile, instability mode I ceases to exist, leaving only mode II. This is consistent with established results which have shown that the classical shear layer type flow has a single unstable mode.

The characteristics of instability mode II are consistent with established characteristics of classical shear layer type flows whose mean profiles are governed by the tanh-type relation. Unless the shear layer region and the velocity deficit region of the wake are merged beyond a certain extent, the stability characteristics of mode I are only affected by changes to the wake part of the velocity profile; by extension, the stability characteristics of mode II are only affected by changes to the shear layer part of the velocity profile.

For configurations having mean velocity profiles with unmerged shear layer and wake regions, the growth rate of mode II is greater than that of mode I. When the shear layer and wake regions start merging, the growth rates of both modes become comparable. When these two regions have merged to a large enough extent, mode I can no longer be independently detected. For the baseline configuration, the Rossiter tone always lies within the range of unstable frequencies. At the lower range of instability frequencies, the growth rates of all the control configurations are nearly identical to that of the baseline. Despite the near-constant growth rates, the suppression results vary greatly as the location of the cylinder is changed. This suggests that the link between the cavity tone suppression and the influence

of the cylinder on the shear layer stability is weak. However, other mechanisms for cavity resonance suppression using the cylinder in crossflow configuration, such as high frequency forcing and shear layer lift-off will need to be examined more closely before a conclusive statement can be made.

-
- ¹ H. H. Heller and W. M. Dobrzynski, "Sound radiation "from" aircraft wheel-well/landing-gear configurations", *Journal of Aircraft* **14**, 768 (1977).
 - ² O. W. McGregor and R. A. White, "Drag of rectangular cavities in supersonic and transonic flow including the effects of cavity resonance", *American Institute of Aeronautics and Astronautics Journal* **18**, 1959 (1970).
 - ³ D. Sahoo, A. M. Annaswamy, and F. Alvi, "Active store trajectory control in supersonic cavities using microjets and low-order modeling", *American Institute of Aeronautics and Astronautics Journal* **45**, 516 (2007).
 - ⁴ R. A. King, T. R. C. Jr., and D. M. Bushnell, "Experimental transition investigation of a free-shear layer above a cavity at mach 3.5", *Journal of Propulsion and Power* **7**, 626 (1991).
 - ⁵ H. N. Najm and A. F. Ghoneim, "Numerical simulation of the convective instability in a dump combustor", *American Institute of Aeronautics and Astronautics Journal* **29**, 911 (1991).
 - ⁶ P. C. Kriesels, M. C. A. M. Peters, A. Hirschberg, A. P. J. Wijnands, A. Iafrati, G. Riccardi, R. Piva, and J. C. Bruggeman, "High amplitude vortex-induced pulsations in a gas transport system", *Journal of Sound and Vibration* **184**, 343 (1995).
 - ⁷ W. W. Martin, M. Padmanabhan, and E. Naudascher, "Fluid-dynamic excitation involving flow instability", *Journal of the Hydraulics Division* **101**, 681 (1975).
 - ⁸ D. Rockwell and E. Naudascher, "Review – self-sustaining oscillations of flow past cavities", *Transactions of the ASME: Journal of Fluids Engineering* **100**, 152 (1978).
 - ⁹ N. Chokani, "Flow induced oscillations in cavities - a critical survey", *DGLR/AIAA 92-01-159* (1992).
 - ¹⁰ L. N. Cattafesta, D. R. Williams, C. W. Rowley, and F. Alvi, "Review of active control of flow-induced cavity resonance", *American Institute of Aeronautics and Astronautics Paper* 2003-3567 (2003).
 - ¹¹ C. W. Rowley and D. R. Williams, "Dynamics and control of high-Reynolds-number flow over

- open cavities", *Annual Review of Fluid Mechanics* **38**, 251 (2006).
- ¹² C. K. W. Tam and K. K. Ahuja, "Theoretical model of discrete tone generation by impinging jets", *Journal Fluid Mechanics* **214**, 67 (1990).
 - ¹³ G. Raman, "Supersonic jet screech: half-century from powell to the present", *Journal of Sound and Vibration* **225**, 543 (1999).
 - ¹⁴ D. G. Crighton, "The jet edge-tone feedback cycle - linear theory for the operating stages", *Journal of Fluid Mechanics* **234**, 361 (1992).
 - ¹⁵ M. S. Howe, "Edge, cavity and aperture tones at very low mach numbers", *Journal of Fluid Mechanics* **330**, 61 (1997).
 - ¹⁶ L. F. East, "Aerodynamically induced resonance in rectangular cavities", *Journal of Sound and Vibration* **3**, 277 (1966).
 - ¹⁷ A. Powell, "On the edgetone", *The Journal of the Acoustical Society of America* **33**, 395 (1961).
 - ¹⁸ J. E. Rossiter, "Wind tunnel experiments on the flow over rectangular cavities at subsonic and transonic speeds", Technical report, Aeronautical Research Council Reports and Memoranda, No. 3438, London, England, 1966.
 - ¹⁹ A. J. Bilanin and E. E. Covert, "Estimation of possible excitation frequencies for shallow rectangular cavities", *American Institute of Aeronautics and Astronautics Journal* **11**, 347 (1973).
 - ²⁰ C. K. W. Tam and P. J. W. Block, "On the tones and pressure oscillations induced by flow over rectangular cavities", *Journal of Fluid Mechanics* **89**, 373 (1978).
 - ²¹ S. Raghu and G. Raman, "Cavity resonance suppression using miniature fluidic oscillators", *American Institute of Aeronautics and Astronautics Journal* **42**, 2608 (2004).
 - ²² S. F. McGrath and L. L. Shaw, "Active control of shallow cavity acoustic resonance", *American Institute of Aeronautics and Astronautics Paper 1996-1949* (1996).
 - ²³ L. S. Ukeiley, M. K. Ponton, J. M. Seiner, and B. Jansen, "Suppression of pressure loads in cavity flows", *American Institute of Aeronautics and Astronautics Journal* **42**, 70 (2004).
 - ²⁴ M. Stanek, G. Raman, V. Kibens, J. Ross, J. Odedra, and J. W. Peto, "Suppression of cavity resonance using high frequency forcing – the characteristic signature of effective devices", *American Institute of Aeronautics and Astronautics Paper 2001-2128* (2001).
 - ²⁵ M. Stanek, G. Raman, J. A. Ross, J. Odedra, J. W. Peto, F. Alvi, and V. Kibens, "High frequency acoustic suppression – the role of mass flow, the notion of superposition, and the role of inviscid instability - a new model (part II)", *American Institute of Aeronautics and*

- Astronautics Paper 2002-2404 (2002).
- ²⁶ M. Stanek, J. A. Ross, J. Odedra, and J. Peto, "High frequency acoustic suppression—the mystery of the rod-in-crossflow revealed", American Institute of Aeronautics and Astronautics Paper 2003-0007 (2003).
 - ²⁷ S. Arunajatesan, J. D. Shipman, and N. Sinha, "Hybrid RANS-LES simulation of cavity flow fields with control", American Institute of Aeronautics and Astronautics Paper 2002-1130 (2002).
 - ²⁸ J. M. Wiltse and A. Glezer, "Direct excitation of small-scale motions in free shear flows", *Physics of Fluids* **10**, 2026 (1998).
 - ²⁹ A. B. Cain, M. M. Rogers, V. Kibens, and G. Raman, "Simulations of high-frequency excitation of a plane wake", American Institute of Aeronautics and Astronautics Paper 2001-0514 (2001).
 - ³⁰ A. B. Cain, M. M. Rogers, and V. Kibens, "Characterization of high-frequency excitation of a wake by simulation", American Institute of Aeronautics and Astronautics Paper 2003-0179 (2003).
 - ³¹ M. Stanek, N. Sinha, J. Seiner, B. Pearce, and M. I. Jones, "High frequency flow control—suppression of aero-optics in tactical direct energy beam propagation and the birth of a new model (part-I)", American Institute of Aeronautics and Astronautics Paper 2002-0272 (2002).
 - ³² L. Lees and E. Reshotko, "Stability of the compressible laminar boundary layer", *Journal of Fluid Mechanics* **12**, 555 (1962).
 - ³³ A. Michalke, "On the inviscid instability of the hyperbolic tangent velocity profile", *Journal of Fluid Mechanics* **19**, 543 (1964).
 - ³⁴ A. Michalke, "On spatially growing disturbances in an inviscid shear layer", *Journal of Fluid Mechanics* **23**, 521 (1965).
 - ³⁵ C. W. Rowley, "Modeling, Simulation, and Control of Cavity Flow Oscillations", PhD thesis, California Institute of Technology, Pasadena, 2002.
 - ³⁶ M. M. Koochesfahani and C. E. Frieler, "Instability of nonuniform density free shear layers with a wake profile", *American Institute of Aeronautics and Astronautics Journal* **27**, 1735 (1989).
 - ³⁷ P. Panickar, "Mode switching and linear stability analysis of resonant acoustic flows", PhD thesis, Illinois Institute of Technology, 2008.
 - ³⁸ A. Michalke, "Survey on jet instability theory", *Progress in Aerospace Sciences* **21**, 159 (1984).
 - ³⁹ M. Gharib and A. Roshko, "The effect of flow oscillations on cavity drag", *Journal of Fluid*

- Mechanics **177**, 501 (1987).
- ⁴⁰ N. Forestier, L. Jacquin, and P. Geffroy, “The mixing layer over a deep cavity at high-subsonic speed”, *Journal of Fluid Mechanics* **475**, 101 (2003).
 - ⁴¹ C. W. Rowley, T. Colonius, and A. J. Basu, “On self-sustained oscillations in two-dimensional compressible flow over rectangular cavities”, *Journal of Fluid Mechanics* **415**, 315 (2002).
 - ⁴² G. Raman, E. Envia, and T. J. Bencic, “Jet-cavity interaction tones”, *American Institute of Aeronautics and Astronautics Journal* **40**, 1503 (2002).
 - ⁴³ J.O. Hinze, “Turbulence” , McGraw-Hill Book Co. (1959).
 - ⁴⁴ C., W., Rowley, D., R., Williams , T., Colonius, R., M., Murray, and D. G. Macmynowski, “Linear Models for Control of Cavity Flow Oscillations”, *Journal of Fluid Mechanics* **547**, 317 (2006).
 - ⁴⁵ S. Sarpotdar, and G. Raman, “Influence of shedding cylinder on cavity flow dynamics”, *American Institute of Aeronautics and Astronautics Paper* 2009-3350(2009).
 - ⁴⁶ M. Bastrzyk, and G. Raman, “Cavity noise suppression through shear layer liftoff”, *American Institute of Aeronautics and Astronautics Paper* 2009-3209(2009).

List of Tables

I	Streamwise and transverse locations of the cylinder for various configurations investigated in the current work.	38
---	--	----

List of Figures

1	Schematic of the cavity resonance generation mechanism.	40
2	Schematic of cavity resonance experiments along with coordinate axes location and orientation (all dimensions are in mm).	41
3	Sample hybrid velocity profile showing the influence of various empirical parametric constants as indicated in equation (7).	42
4	Comparison between experimentally observed Strouhal number of the dominant instability in the current experiments and Rossiter's phase locking formula given in equation (1).	43
5	Comparison between spectra for the baseline and two representative control configurations, $M = 0.6$. For suppression cases A.2 and A.4, cylinder is located at $x/d = -1.59, g/d = 1.43$ and $x/d = -6.35, g/d = 1.43$ respectively.	44
6	Acoustic characteristics of the baseline configuration.	45
7	Suppression characteristics of the various control configurations. (a). Streamwise locations 'A' (refer Table I) of cylinder at $x/d = -1.59$, (b). Streamwise locations 'B' (refer Table I) of cylinder at $x/d = -6.35$	46
8	Mean velocity distribution and pressure eigenfunctions of the instability modes of the A.5 configuration (principal profile). (a). (\circ) experimentally measured mean velocity, (—) best-fitting curve according to equation (7), and values of profile parameters for this principal profile, (b), (c). Sample eigenfunctions at $\omega = 5.59$ ($St = 0.89$), $M = 0.6$. (b). Instability mode I, $\alpha = -12.68 - 2.17i$, (c). Instability mode II, $\alpha = -11.04 - 5.27i$. The pressure eigenfunctions are normalized such that $\max[\hat{p}] = 1$	47
9	Effect of changing the wake amplitude parameter, W_{amp} , in equation (7) on the stability characteristics of modes I and II. (a). Sample hybrid mean velocity profiles showing the effect of changing W_{amp} , (b). Instability growth rates and phase velocities for mode I, (c). Instability growth rates and phase velocities for mode II.	48

10	Effect of changing the wake width parameter, W_{wid} , in equation (7) on the stability characteristics of modes I and II. (a). Sample hybrid mean velocity profiles showing the effect of changing W_{wid} , (b). Instability growth rates and phase velocities for mode I, (c). Instability growth rates and phase velocities for mode II.	49
11	Effect of changing the wake offset parameter, W_{off} , in equation (7) on the stability characteristics of modes I and II. (a). Sample hybrid mean velocity profiles showing the effect of changing W_{off} , (b). Instability growth rates and phase velocities for mode I, (c). Instability growth rates and phase velocities for mode II.	50
12	Instability growth rates of the first two Rossiter modes as a function of the vorticity thickness, δ_w	51
13	Effect of changing the vorticity thickness parameter, δ_w , in equation (7) on the stability characteristics of modes I and II. (a). Sample hybrid mean velocity profiles showing the effect of changing δ_w , (b). Instability growth rates and phase velocities for mode I, (c). Instability growth rates and phase velocities for mode II.	52
14	Experimentally measured mean velocities (o) fitted using the equation for the classical tanh-type profile (6) or the hybrid profile (7) (—), as applicable. Starting at the bottom, which shows the baseline profile, each successive mean profile is shifted by one unit in the transverse (Y) direction in order to facilitate ease of viewing. (a). Mean profiles and curve fits for locations 'A.×' in Table I, (b). Mean profiles and curve fits for locations 'B.×' in table I. Profiles measured at $z = 0$, $x = 0.08$ for $M = 0.60$	53
15	Experimentally measured mean velocities (o) at various streamwise locations, fitted using the equation for the classical tanh-type profile (6) or the hybrid profile (7) (—), as applicable. (a). Baseline configuration, (b). Configuration A.1, (c). Configuration A.2, (d). Configuration A.4, (e). Configuration A.6. Profiles measured along the streamwise direction at $z = 0$ for $M = 0.60$. Refer to Table I for the configurational details.	54

16	Instability growth rates of (a). Mode I, and (b). Mode II, for the curve fits to the experimentally measured mean velocities shown in figure 14(a). Refer to Table I for configurational details.	56
17	Instability growth rates of (a). Mode I, and (b). Mode II, for the curve fits to the experimentally measured mean velocities shown in figure 14(b). Refer to Table I for configurational details.	57
18	Maximum growth rate of instability mode II of experimentally measured profiles and synthetic profiles as a function of the vorticity thickness parameter δ_w	58
19	Integrated growth rates of instability modes I and II for the first two Rossiter mode frequencies. Refer to Table I for the configurational details.	59

Tables

Configuration	x/d	g/d
A.1	-1.59	0.50
A.2	-1.59	1.43
A.3	-1.59	1.48
A.4	-1.59	1.76
A.5	-1.59	3.15
A.6	-1.59	4.40
B.1	-6.35	0.50
B.2	-6.35	1.43
B.3	-6.35	1.48
B.4	-6.35	1.76
B.5	-6.35	3.15
B.6	-6.35	4.40

TABLE I: Streamwise and transverse locations of the cylinder for various configurations investigated in the current work.

Figures

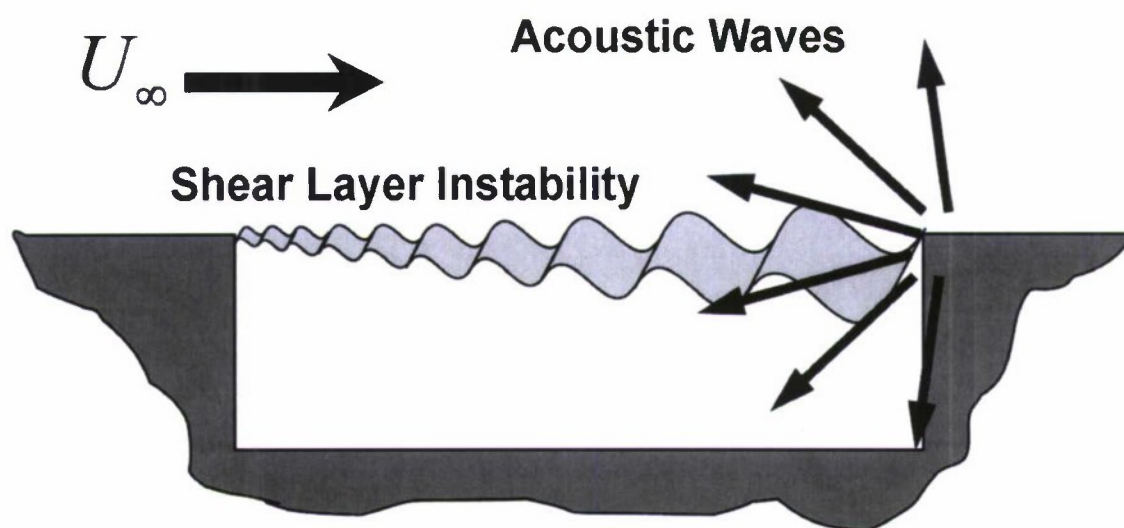


FIG. 1: Schematic of the cavity resonance generation mechanism.

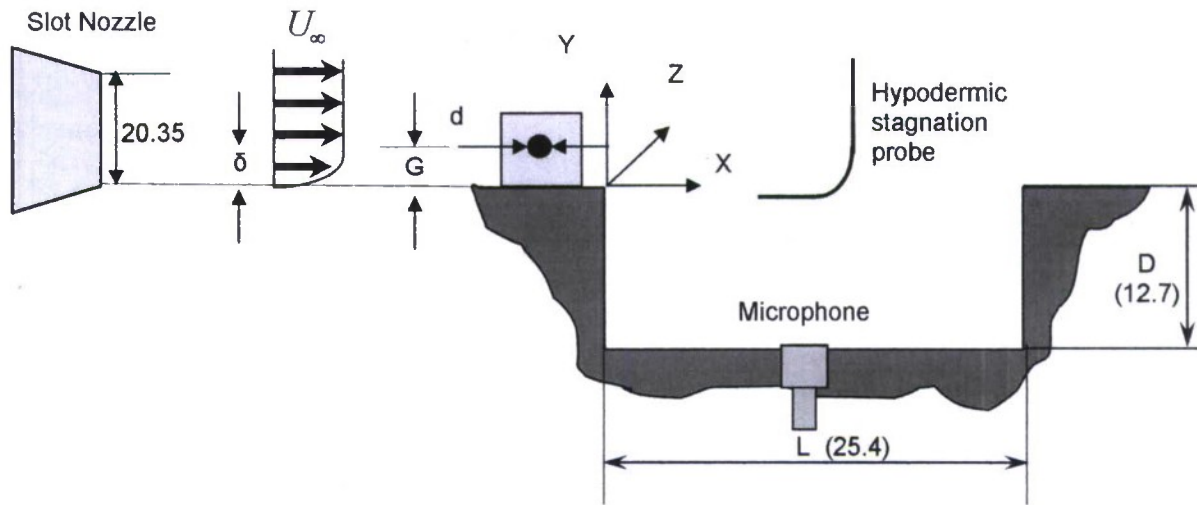


FIG. 2: Schematic of cavity resonance experiments along with coordinate axes location and orientation (all dimensions are in mm).

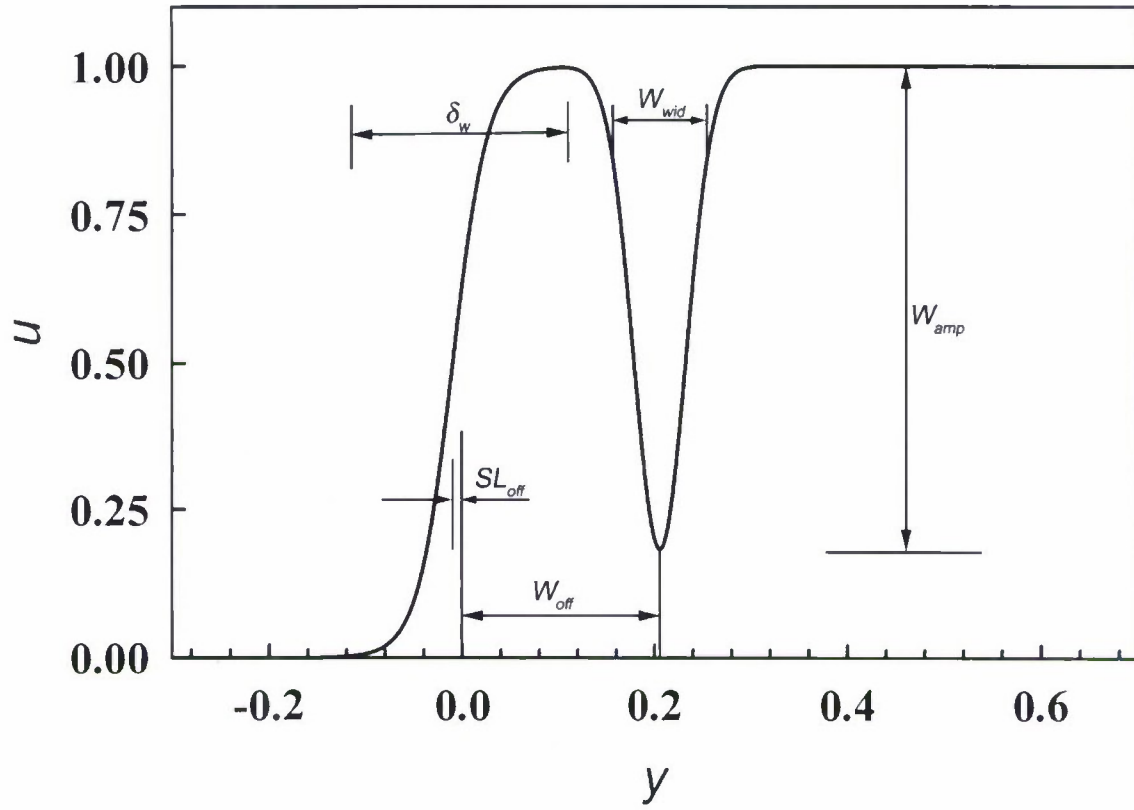


FIG. 3: Sample hybrid velocity profile showing the influence of various empirical parametric constants as indicated in equation (7).

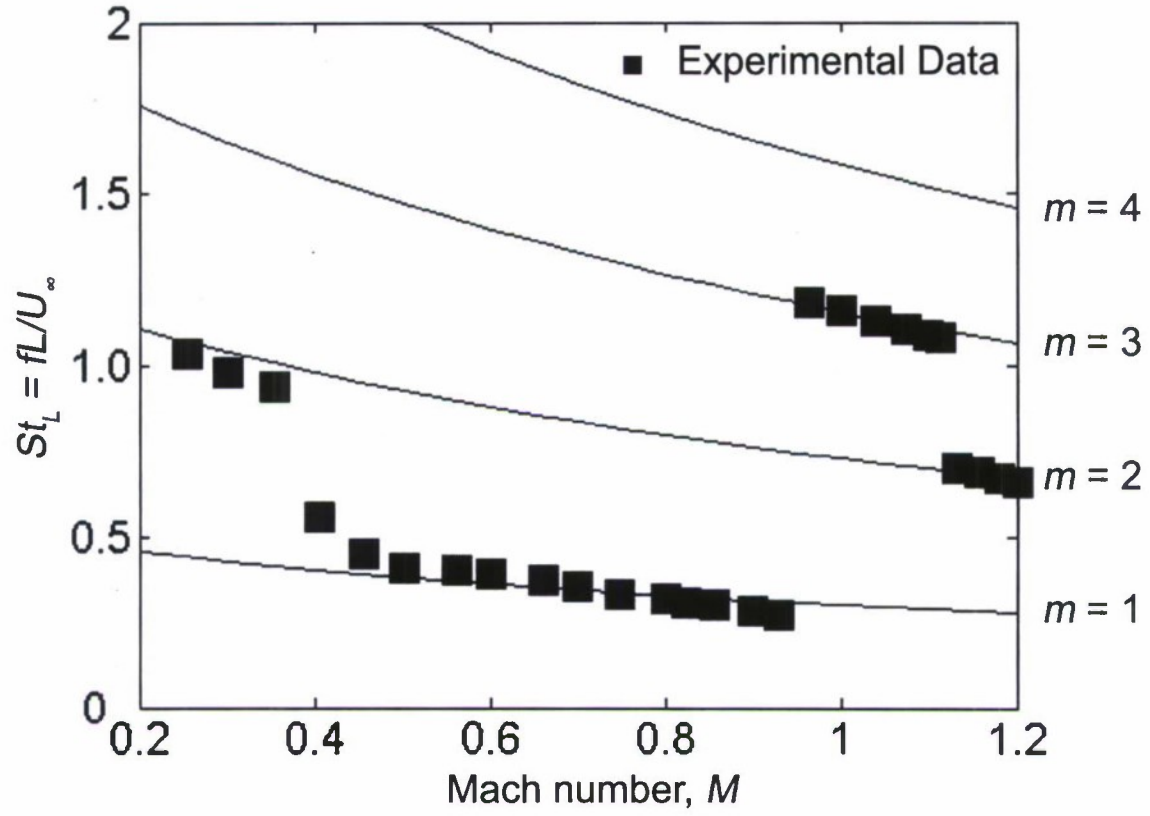


FIG. 4: Comparison between experimentally observed Strouhal number of the dominant instability in the current experiments and Rossiter's phase locking formula given in equation (1).

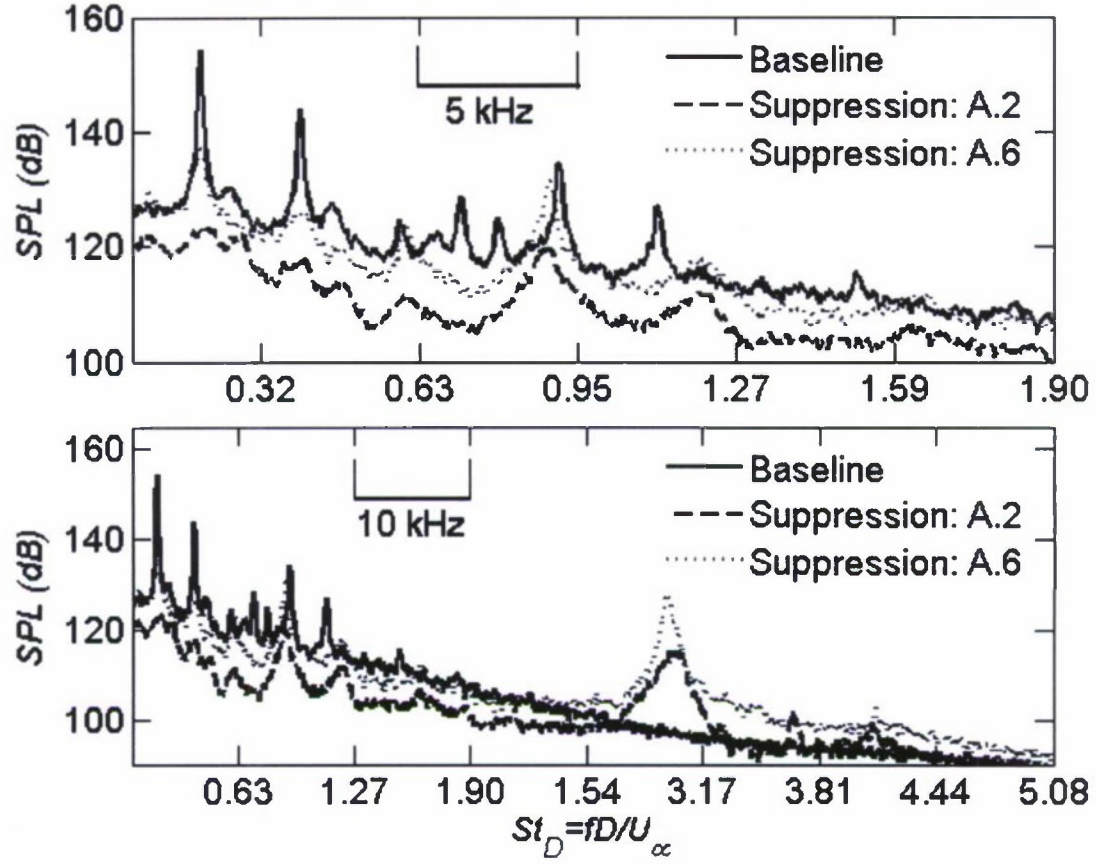


FIG. 5: Comparison between spectra for the baseline and two representative control configurations, $M = 0.6$. For suppression cases A.2 and A.4, cylinder is located at $x/d = -1.59, g/d = 1.43$ and $x/d = -6.35, g/d = 1.43$ respectively.

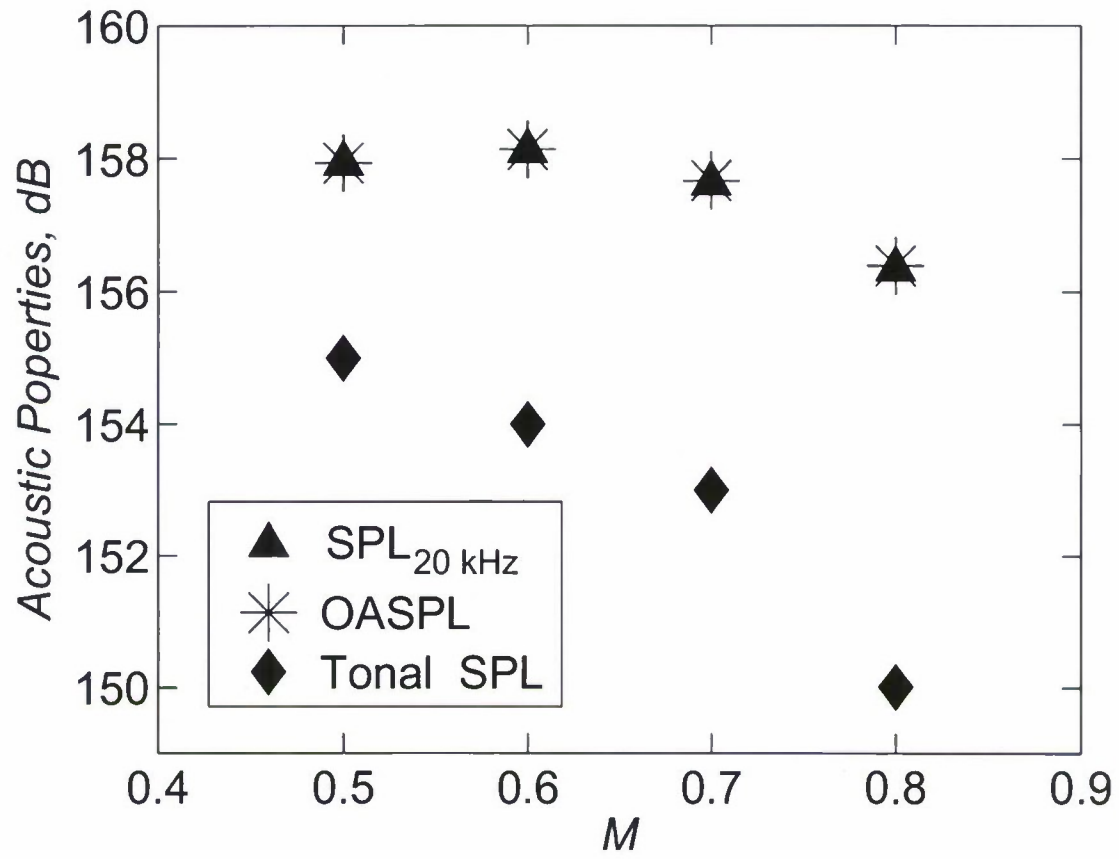


FIG. 6: Acoustic characteristics of the baseline configuration.

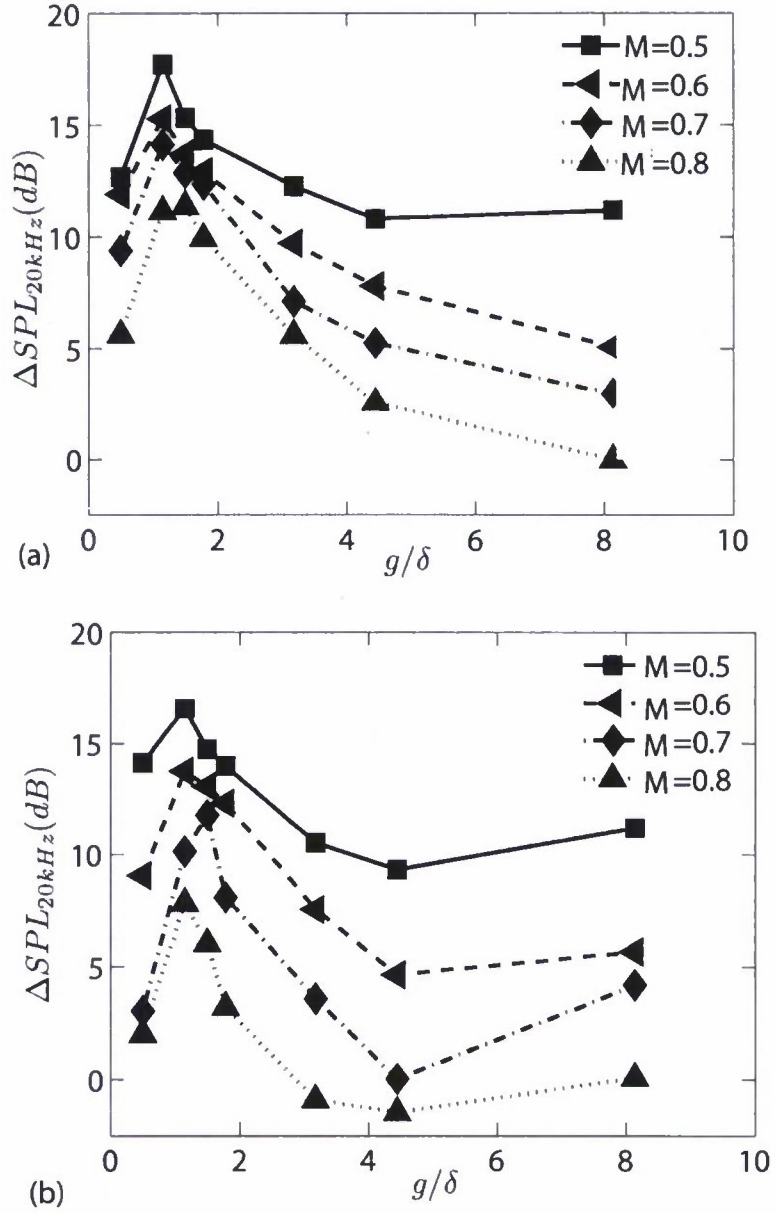


FIG. 7: Suppression characteristics of the various control configurations. (a). Streamwise locations 'A' (refer Table I) of cylinder at $x/d = -1.59$, (b). Streamwise locations 'B' (refer Table I) of cylinder at $x/d = -6.35$.

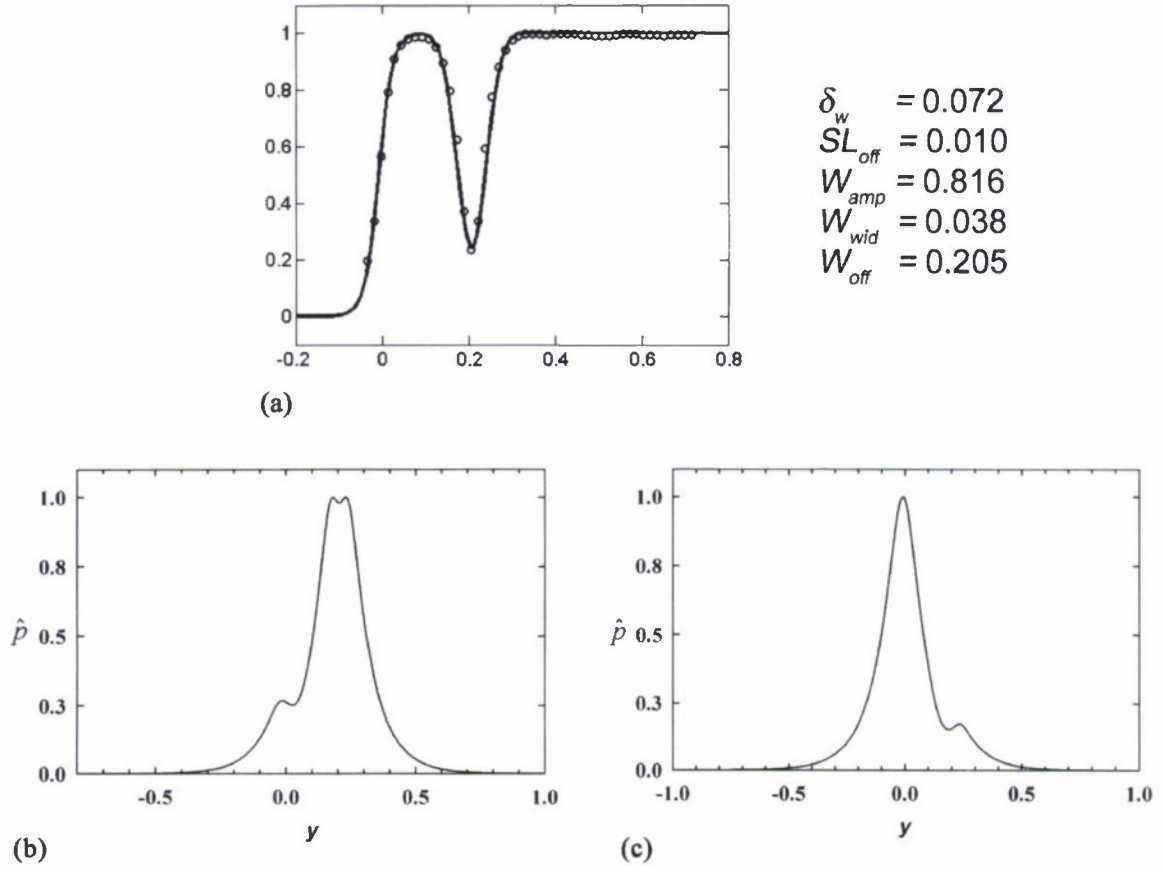


FIG. 8: Mean velocity distribution and pressure eigenfunctions of the instability modes of the A.5 configuration (principal profile). (a). (o) experimentally measured mean velocity, (—) best-fitting curve according to equation (7), and values of profile parameters for this principal profile, (b), (c). Sample eigenfunctions at $\omega = 5.59$ ($St = 0.89$), $M = 0.6$. (b). Instability mode I, $\alpha = -12.68 - 2.17i$, (c). Instability mode II, $\alpha = -11.04 - 5.27i$. The pressure eigenfunctions are normalized such that $\max[\hat{p}] = 1$.

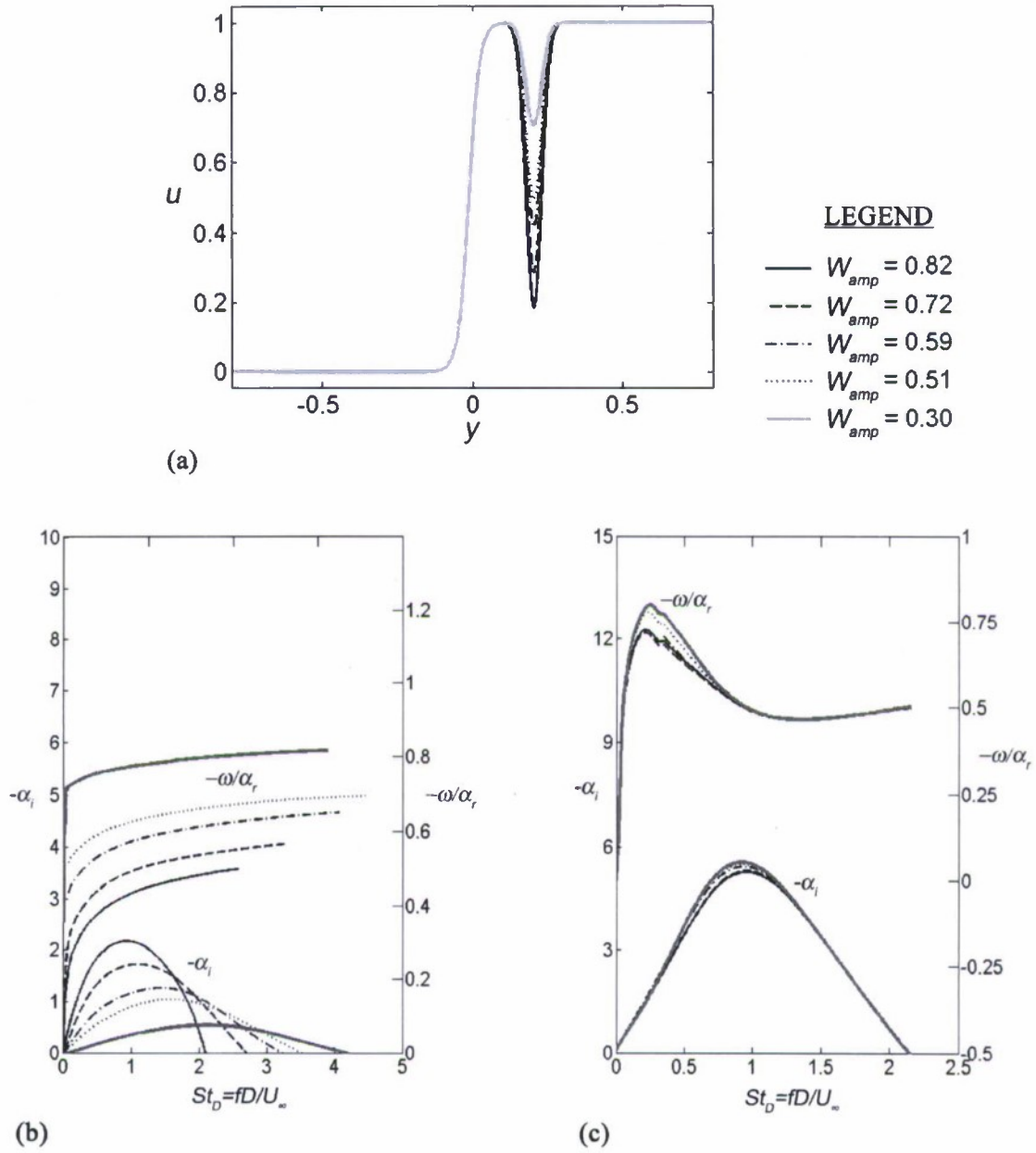


FIG. 9: Effect of changing the wake amplitude parameter, W_{amp} , in equation (7) on the stability characteristics of modes I and II. (a). Sample hybrid mean velocity profiles showing the effect of changing W_{amp} , (b). Instability growth rates and phase velocities for mode I, (c). Instability growth rates and phase velocities for mode II.

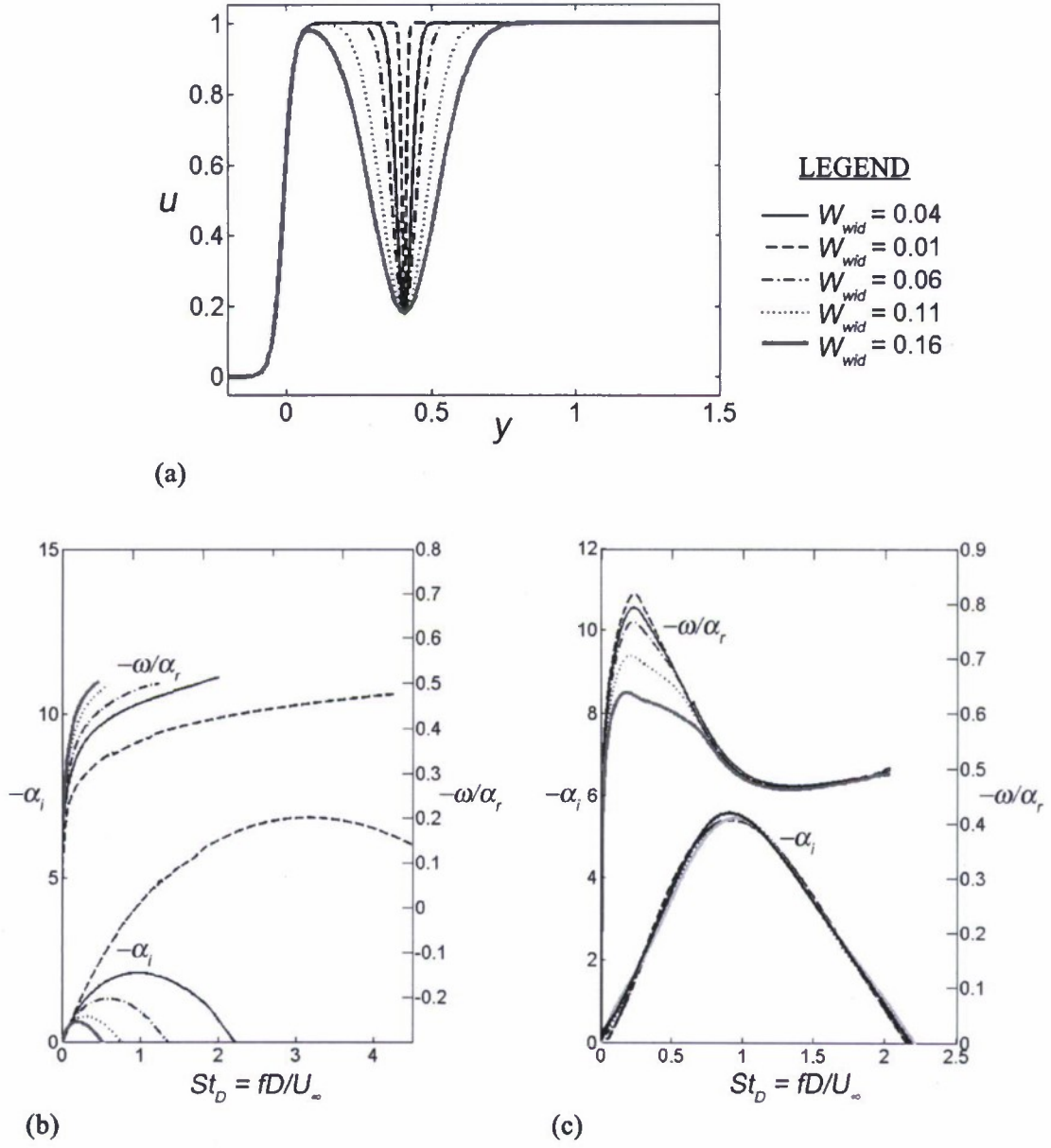


FIG. 10: Effect of changing the wake width parameter, W_{wid} , in equation (7) on the stability characteristics of modes I and II. (a). Sample hybrid mean velocity profiles showing the effect of changing W_{wid} , (b). Instability growth rates and phase velocities for mode I, (c). Instability growth rates and phase velocities for mode II.

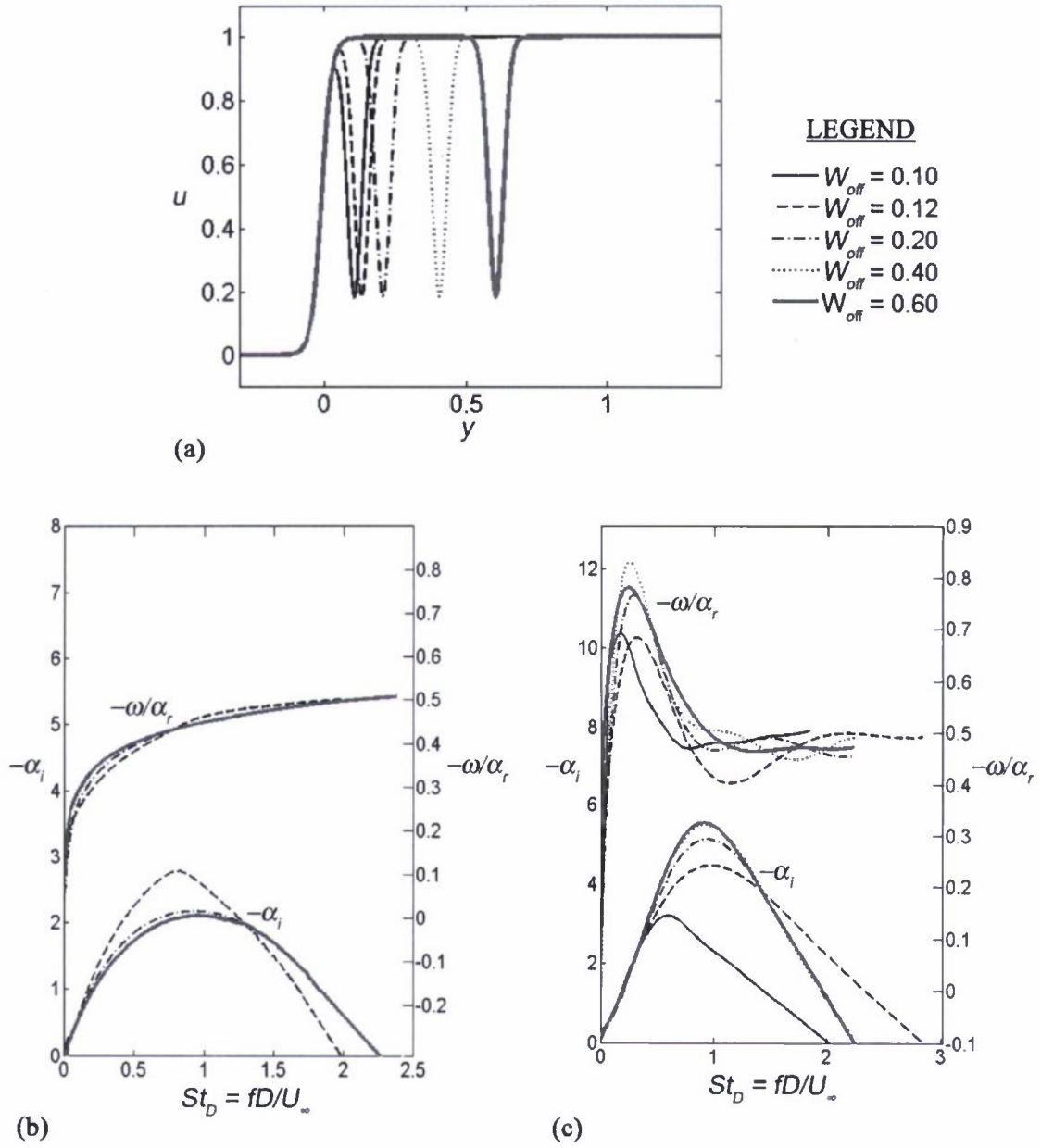


FIG. 11: Effect of changing the wake offset parameter, W_{off} , in equation (7) on the stability characteristics of modes I and II. (a). Sample hybrid mean velocity profiles showing the effect of changing W_{off} , (b). Instability growth rates and phase velocities for mode I, (c). Instability growth rates and phase velocities for mode II.

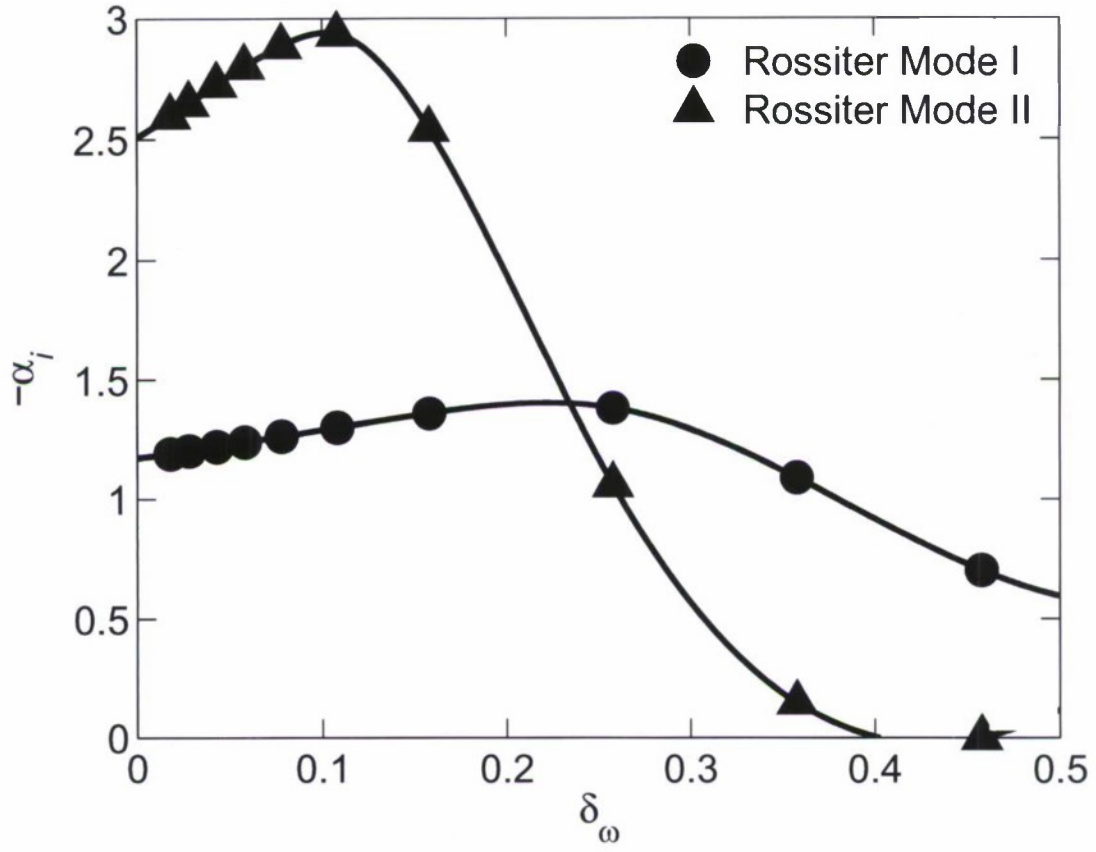


FIG. 12: Instability growth rates of the first two Rossiter modes as a function of the vorticity thickness, δ_w .

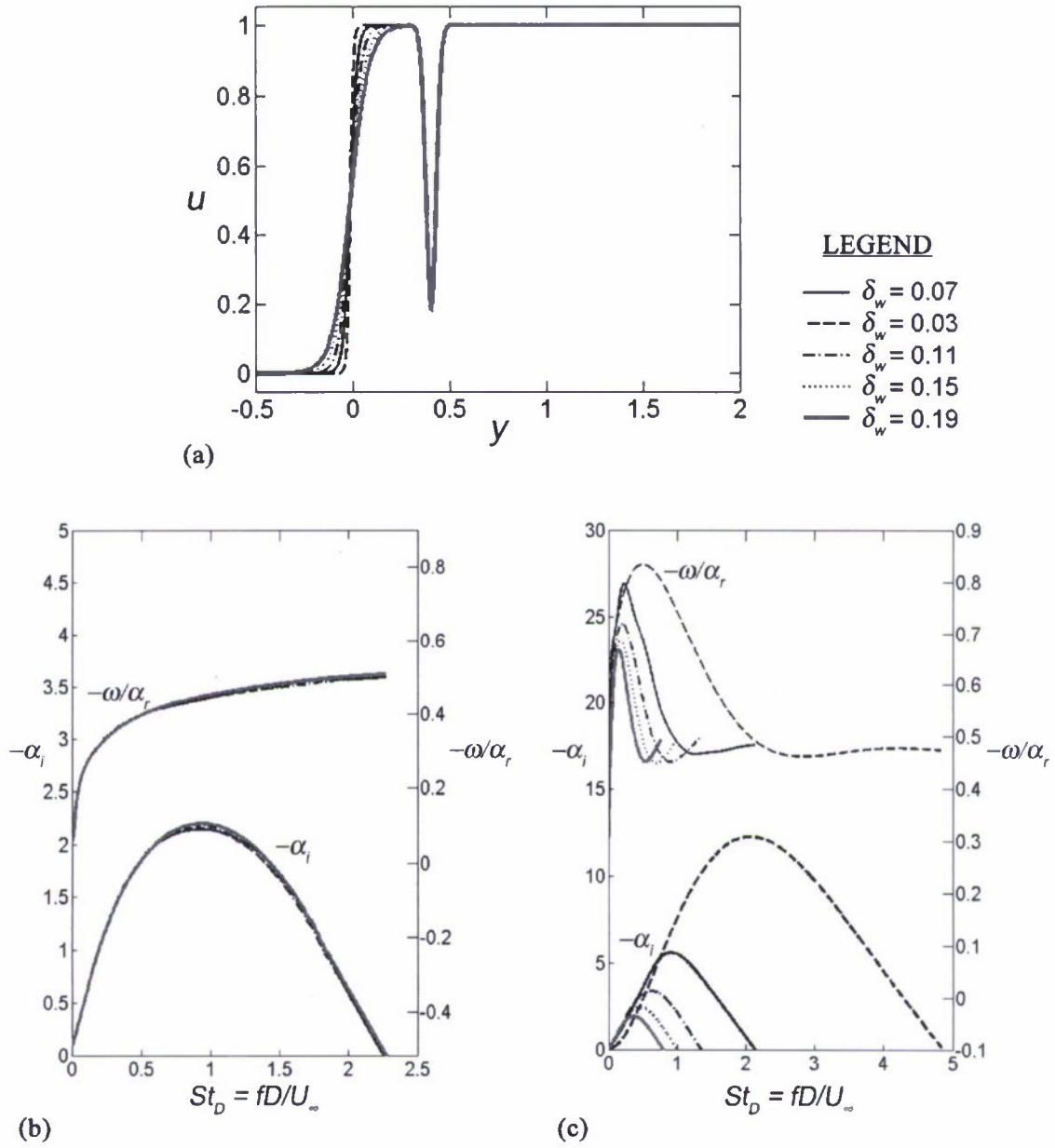


FIG. 13: Effect of changing the vorticity thickness parameter, δ_w , in equation (7) on the stability characteristics of modes I and II. (a). Sample hybrid mean velocity profiles showing the effect of changing δ_w , (b). Instability growth rates and phase velocities for mode I, (c). Instability growth rates and phase velocities for mode II.

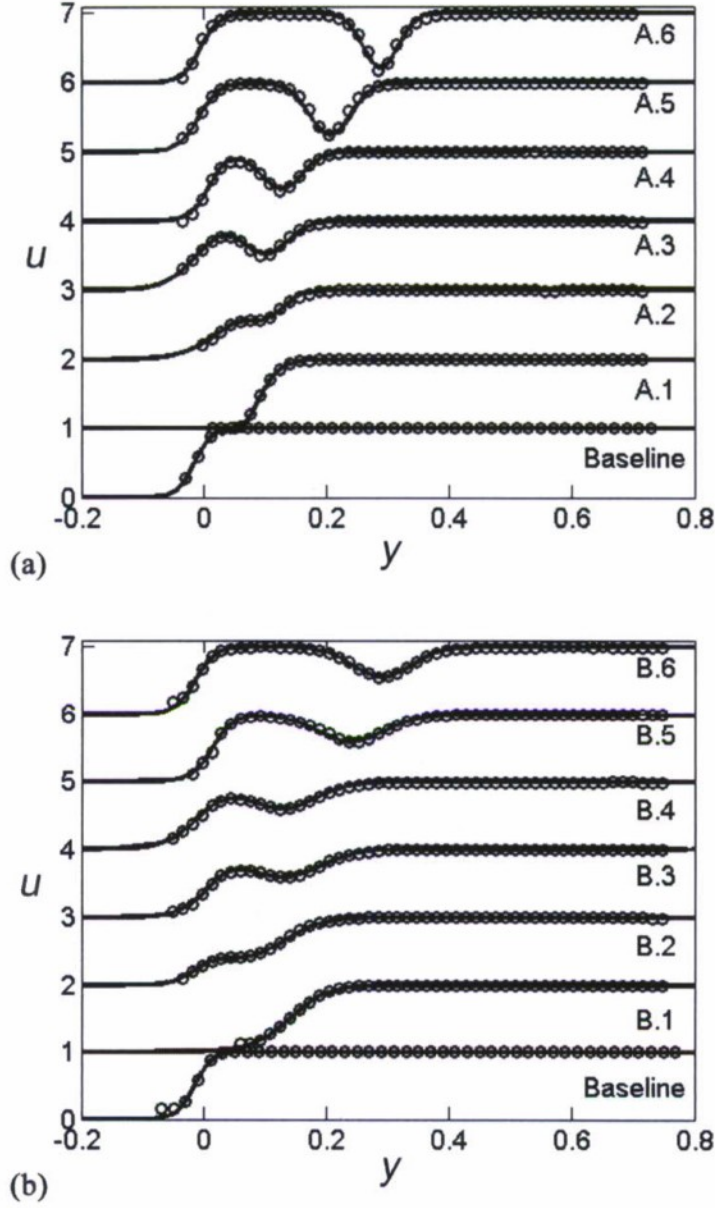


FIG. 14: Experimentally measured mean velocities (\circ) fitted using the equation for the classical tanh-type profile (6) or the hybrid profile (7) (—), as applicable. Starting at the bottom, which shows the baseline profile, each successive mean profile is shifted by one unit in the transverse (Y) direction in order to facilitate ease of viewing. (a). Mean profiles and curve fits for locations 'A. \times ' in Table I, (b). Mean profiles and curve fits for locations 'B. \times ' in table I. Profiles measured at $z = 0$, $x = 0.08$ for $M = 0.60$.

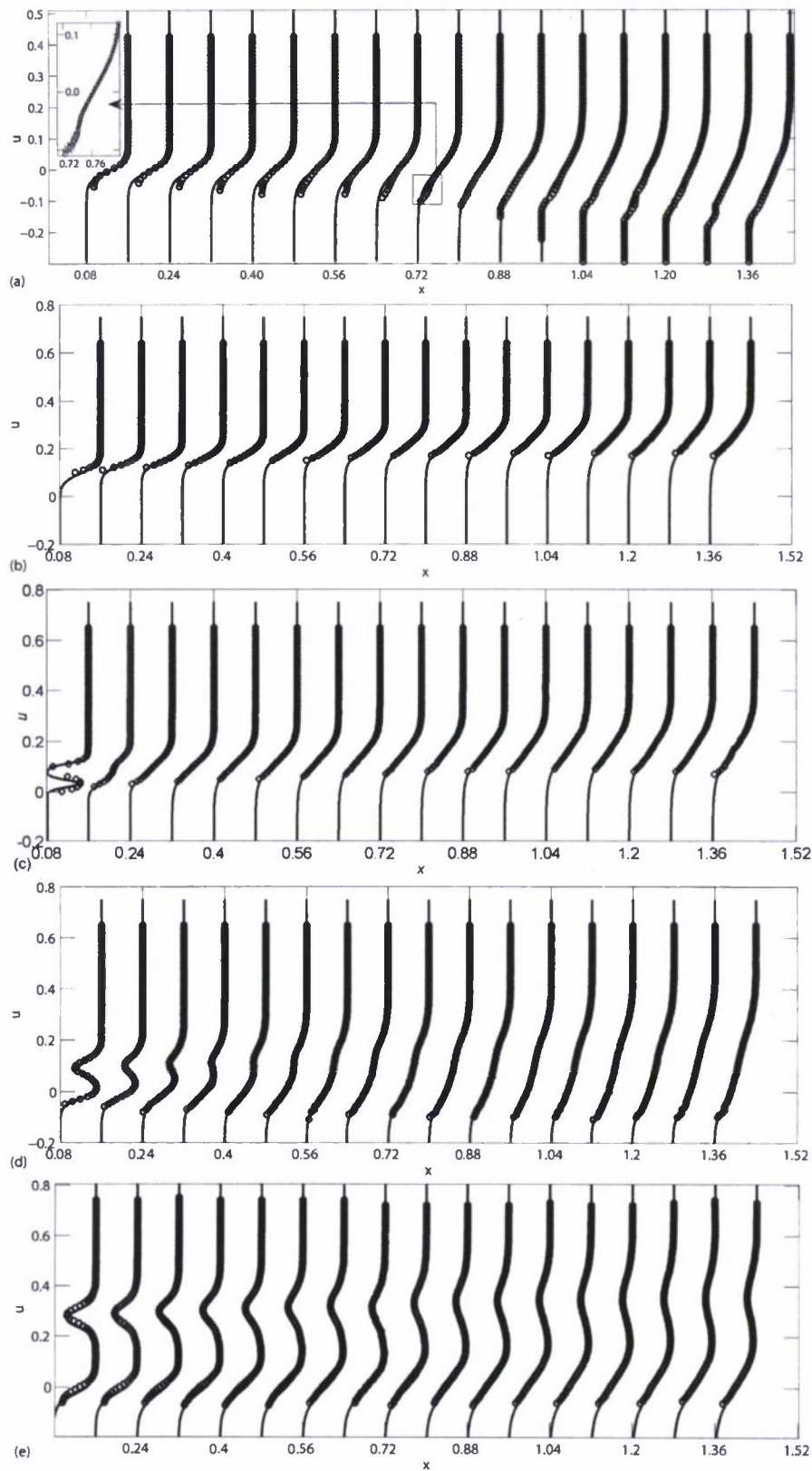


FIG. 15: Experimentally measured mean velocities (\circ) at various streamwise locations, fitted using the equation for the classical tanh-type profile (6) or the hybrid profile (7) (—), as applicable. (a). Baseline configuration, (b). Configuration A.1, (c). Configuration A.2, (d). Configuration A.4, (e). Configuration A.6. Profiles measured along the streamwise direction at $z = 0$ for $M = 0.60$. Refer to Table I for the configurational details.

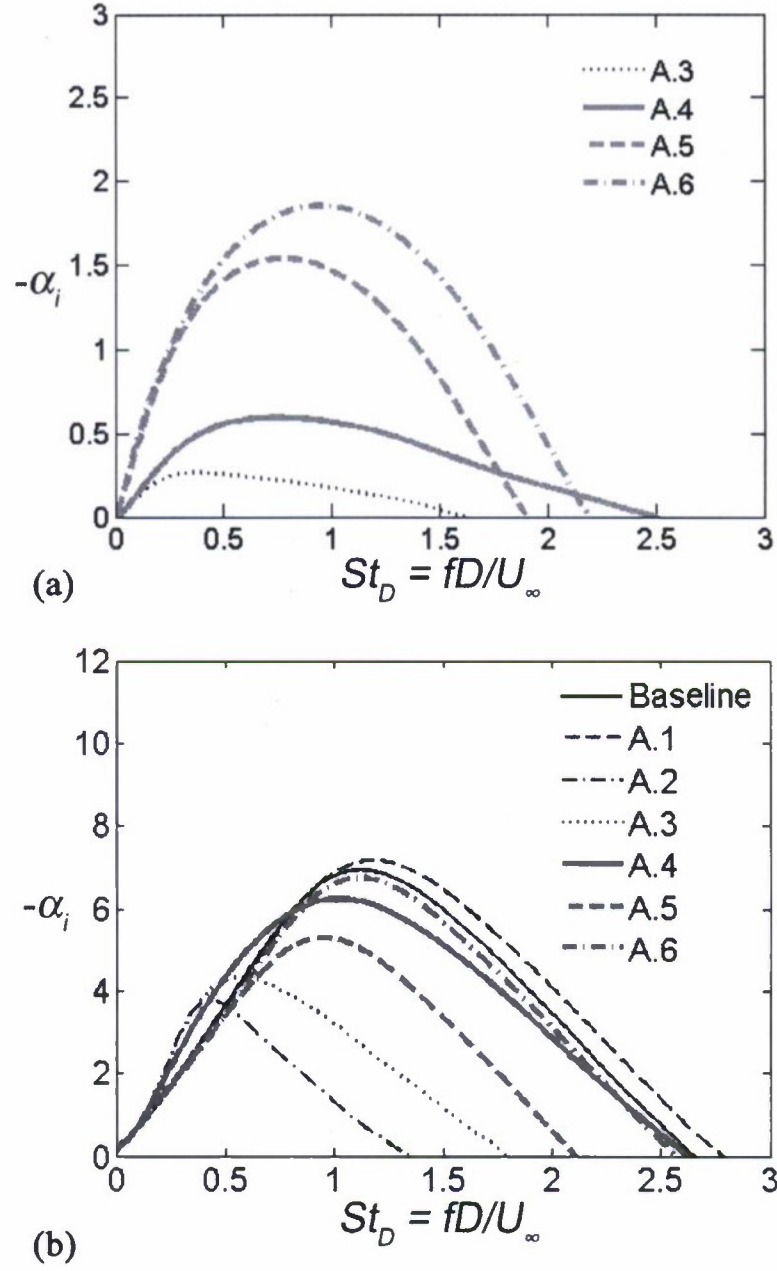


FIG. 16: Instability growth rates of (a). Mode I, and (b). Mode II, for the curve fits to the experimentally measured mean velocities shown in figure 14(a). Refer to Table I for configurational details.

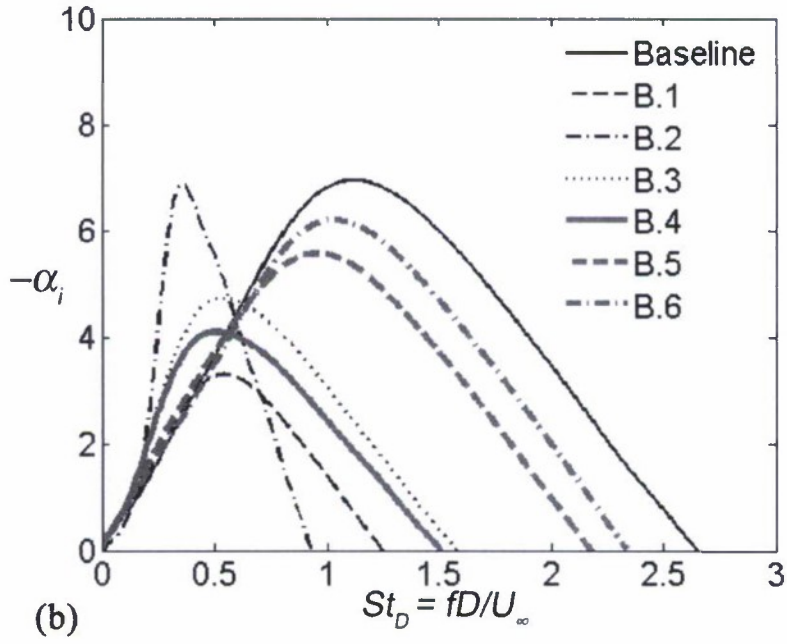
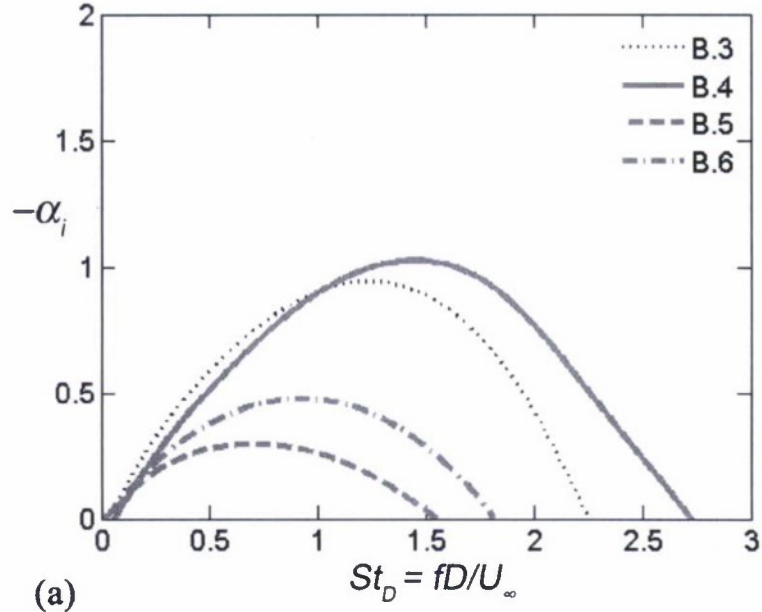


FIG. 17: Instability growth rates of (a). Mode I, and (b). Mode II, for the curve fits to the experimentally measured mean velocities shown in figure 14(b). Refer to Table I for configurational details.

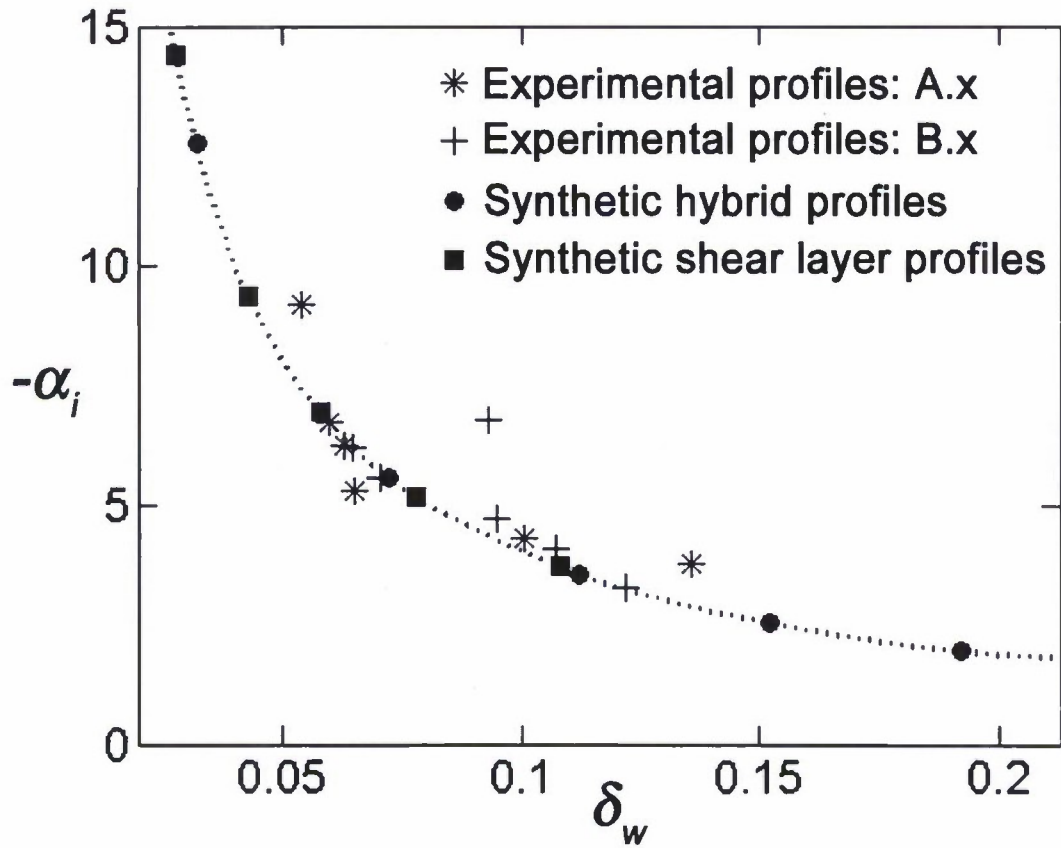


FIG. 18: Maximum growth rate of instability mode II of experimentally measured profiles and synthetic profiles as a function of the vorticity thickness parameter δ_w .

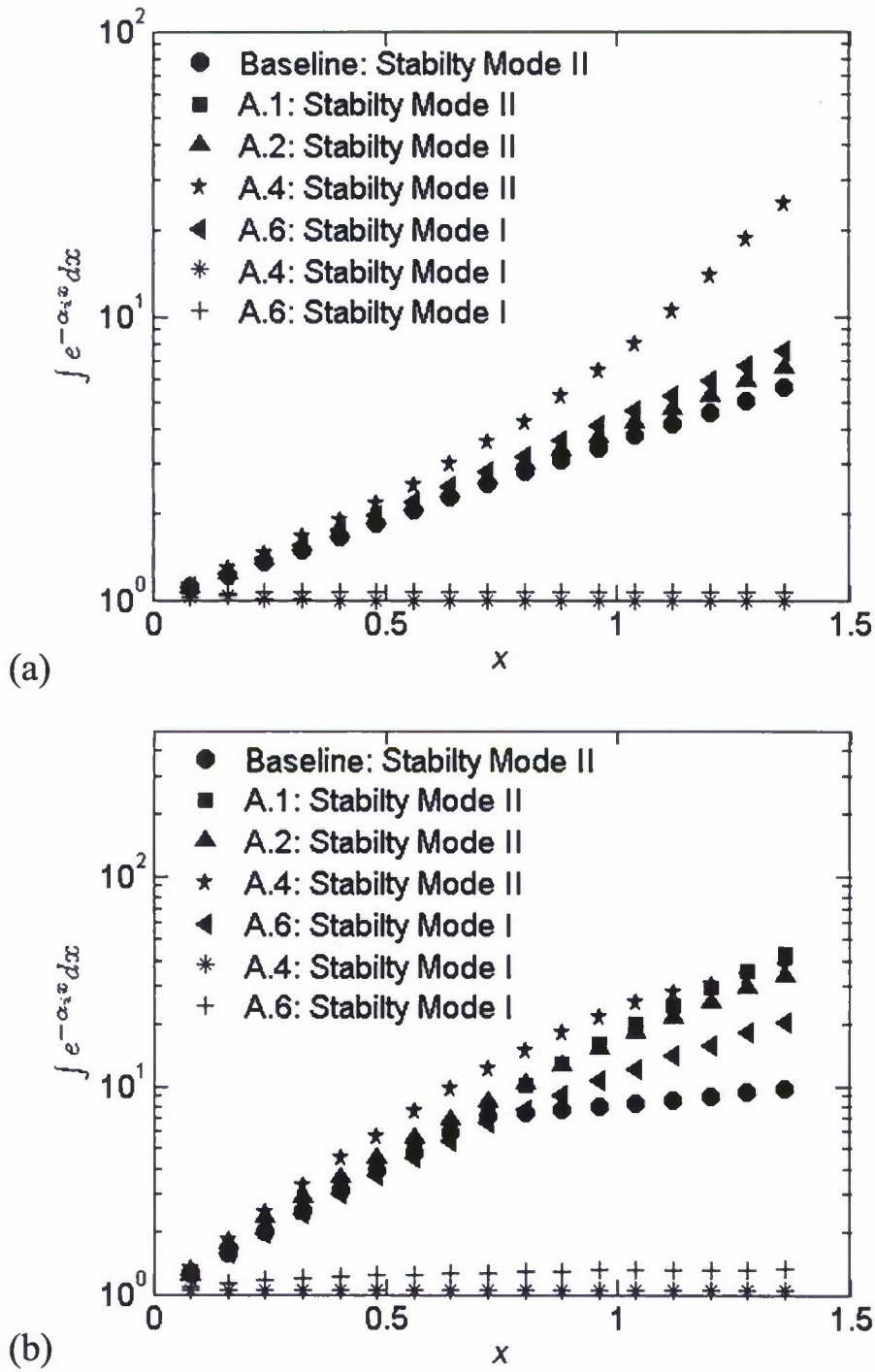


FIG. 19: Integrated growth rates of instability modes I and II for the first two Rossiter mode frequencies. Refer to Table I for the configurational details.